

Rough faults, distributed weakening, and off-fault deformation

W. Ashley Griffith,^{1,3} Stefan Nielsen,¹ Giulio Di Toro,^{1,2} and Steven A. F. Smith¹

Received 28 August 2009; revised 20 December 2009; accepted 25 February 2010; published 24 August 2010.

[1] We report systematic spatial variations in fault rocks along nonplanar strike-slip faults cross-cutting the Lake Edison Granodiorite, Sierra Nevada, California (Sierran wavy fault) and Lobbia outcrops of the Adamello Batholith in the Italian Alps (Lobbia wavy fault). In the case of the Sierran fault, pseudotachylyte formed at contractional fault bends, where it is found as thin (1–2 mm) fault-parallel veins. Epidote and chlorite developed in the same seismic context as the pseudotachylyte and are especially abundant in extensional fault bends. We argue that the presence of fluids, as illustrated by this example, does not necessarily preclude the development of frictional melt. In the case of the Lobbia fault, pseudotachylyte thickness varies along the length of the fault, but the pseudotachylyte veins thicken and pool in extensional bends. We conduct a quantitative analysis of fault roughness, microcrack distribution, stress, and friction along the Lobbia fault. Numerical modeling results show that opening in extensional bends and localized thermal weakening in contractional bends counteract resistance encountered by fault waviness, resulting in an overall weaker fault than suggested by the corresponding static friction coefficient. The models also predict static stress redistribution around bends in the faults which is consistent with distribution of microcracks, indicating significant elastic and inelastic strain energy is dissipated into the wall rocks due to nonplanar fault geometry. Together these observations suggest that damage and energy dissipation occurs along the entire nonplanar fault during slip, rather than being confined to the region close to the dynamically propagating crack tip.

Citation: Griffith, W. A., S. Nielsen, G. Di Toro, and S. A. F. Smith (2010), Rough faults, distributed weakening, and off-fault deformation, *J. Geophys. Res.*, 115, B08409, doi:10.1029/2009JB006925.

1. Introduction

[2] Faults in nature are rough at wavelengths from microns to tens of kilometers [e.g., Power *et al.*, 1987; Saucier *et al.*, 1992; Lee and Bruhn, 1996; Sagy *et al.*, 2007; Candela *et al.*, 2009]. Power *et al.* [1987] showed that natural fractures are self-affine in their roughness across almost 11 orders of magnitude, but faults tend to be smoothest in the slip-parallel direction. Fault roughness causes local variations in the stress and displacement fields near the fault, so the deformation pattern may deviate significantly from that expected of a straight fault [e.g., Berger and Johnson, 1980; Saucier *et al.*, 1992; Chester and Fletcher, 1997; Chester and Chester, 2000], and significant waviness or kinking in fault surfaces may act as a barrier to rupture growth [e.g., Nielsen and Knopoff, 1998; Kame *et al.*, 2003; Bhat *et al.*, 2004]. Okubo and Dieterich [1984] showed experimental evidence for lower rupture velocities, higher critical slip weakening distance, and larger fracture energies for slip on rough (rms roughness = 80 μm) versus smooth (rms roughness = 0.2 μm)

fault surfaces. On a crustal scale, irregular fault geometry appears to control the spatial pattern of earthquake activity [Parsons, 2007]. Clearly, nonuniformity in the referential coordinates caused by rough or “wavy” fault surfaces exerts an important control on the parameters affecting fault friction.

[3] Here we make a connection between nonplanar fault geometry and frictional processes on natural faults by (1) documenting the spatial distribution of fault rock structures along exhumed wavy faults which contain variable amounts of pseudotachylyte (PT) distributed along strike; (2) measuring the spatial distribution and orientation of microcracks in the wall rock; (3) quantitatively measuring the geometry of the faults, including fault surface roughness and pseudotachylyte thickness and volume; (4) evaluating the contribution of multiscale roughness to the fault mechanics and frictional behavior at the fault interface; and (5) attempting to generalize the interplay between frictional processes and irregular fault geometry.

[4] We describe in detail a well-exposed (i.e., glacier polished outcrops) wavy fault in PT-rich faults of the Gole Larghe fault zone (the Lobbia wavy fault) in the southern Italian Alps [e.g., Di Toro and Pennacchioni, 2005] and a wavy fault in the PT-poor faults of the Bear Creek drainage in the Mount Abbot Quadrangle, central Sierra Nevada, California (Sierran wavy fault) [Griffith *et al.*, 2008, 2009a; Kirkpatrick *et al.*, 2008; Kirkpatrick and Shipton, 2009]. The

¹Istituto Nazionale di Geofisica e Vulcanologia, Rome, Italy.

²Dipartimento di Geoscienze, Università di Padova, Padova, Italy.

³Now at the Department of Geology and Environmental Science, University of Akron, Akron, Ohio, USA.

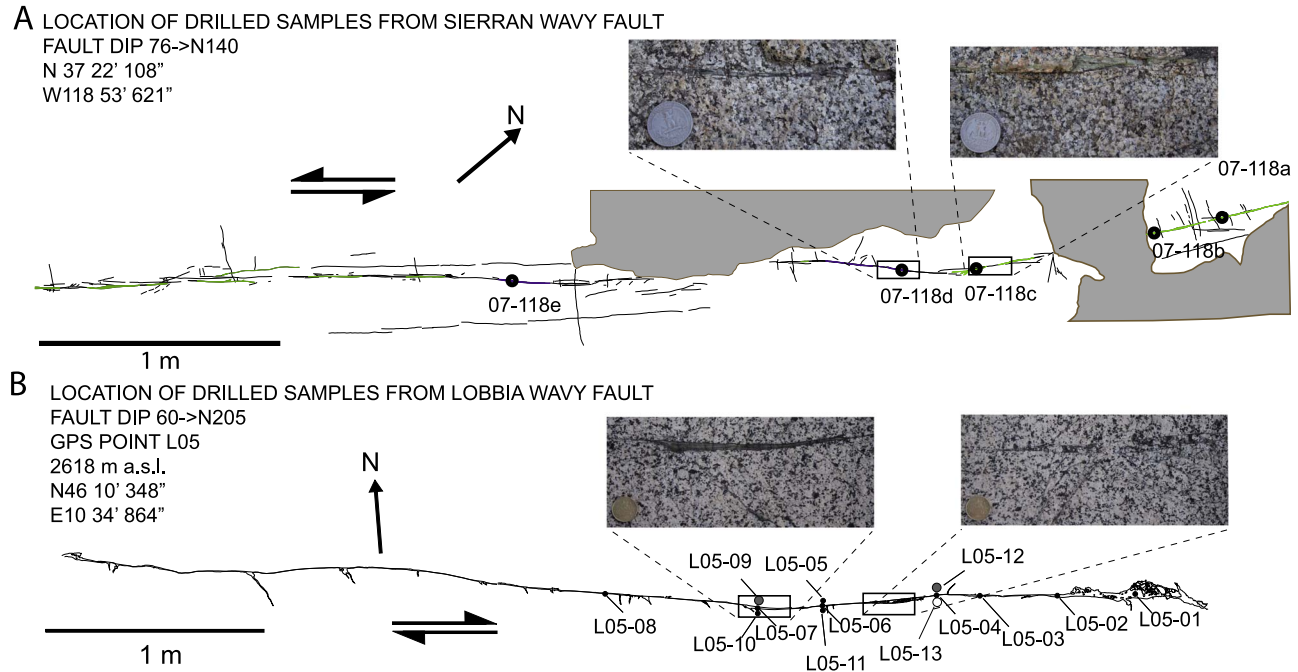


Figure 1. Wavy fault maps of (a) the Sierran wavy fault and (b) the Lobbia wavy fault with sample locations and field photos.

presence of PT on these faults indicates that both faults were seismically active. We mapped and sampled each fault in detail (Figure 1). Field observations indicate that PT was formed preferentially in contractional bends in both faults, and fault rock microstructures vary systematically with the macrostructural geometry of the faults [Kirkpatrick and Shipton, 2009]. We analyze quantitative field data using a quasistatic mechanical numerical model that sheds light on the interplay between friction, stress state, fault surface displacements, and off-fault deformation.

2. Description of Wavy Faults in the Field

2.1. Geologic Background

[5] Faults of the Bear Creek area of the Mount Abbot Quadrangle, Sierra Nevada, California have received considerable attention during the past three decades as a natural laboratory for investigations of fault mechanics in granitoid rocks [e.g., Segall and Pollard, 1983; Martel et al., 1988; Evans et al., 2000; Pachell and Evans, 2002]. Thin PT veins were discovered along some of these faults more recently, implying that these faults can be used to study seismic slip [Griffith et al., 2008, 2009a, 2009b; Kirkpatrick et al., 2008; Kirkpatrick and Shipton, 2009]. In just the last decade, abundant evidence has been reported for seismic (earthquake) slip on fault strands of the Gole Larghe fault zone in the Adamello batholith, Southern Alps, Italy [Di Toro and Pennacchioni, 2004, 2005; Di Toro et al., 2005a, 2005b]. These fault locales are similar in host rock lithology (tonalite), fault rock mineralogy (greenschist facies minerals), and evolution: faults in both locales formed at seismogenic depths (8–12 km) under similar ambient conditions (~250°C) during cooling of the host granitoid rocks and slip events nucle-

ated along preexisting networks of subparallel joints [e.g., Segall and Pollard, 1983; Martel et al., 1988; Di Toro and Pennacchioni, 2004; Griffith et al., 2008].

2.2. Field Observations

[6] Wavy faults in both locales are exposed along a ~5 m trace. In the case of the Lobbia, the fault segment was selected because the outcrop surface was orthogonal to fault dip and subparallel to the direction of slip. In both cases, the fault tips are not exposed; therefore, the actual fault length is unknown. Typical single small faults in the Bear Creek outcrops are between 10 and 20 m in length, whereas single fault strands in the Lobbia can be traced between 10 and 100 m. In the Lobbia, fault strands typically anastomose and link with other fault strands; therefore, the effective length of a fault in the Lobbia outcrops can be >1 km. In the left-lateral Sierran wavy fault (Figure 1a), PT is confined to contractional bends, while extensional bends are filled with hydrothermal minerals [e.g., Griffith et al., 2009a]. Bleaching is observed along the extensional bends, suggesting hydrothermal alteration of plagioclase to form saussurite (epidote + white mica). In the right-lateral Lobbia wavy fault (Figure 1b), PT veins are continuous along strike and form reservoirs, notably at extensional bends. PT injection veins are oriented at high angles to the fault and occur preferentially on the south side of the fault, although they do occur on the north side in a few cases [Di Toro et al., 2005b]. In this selected wavy fault segment, no alteration of the wall rocks is observed; precursory cataclasite on the fault is a very minor component of the fault rocks relative to PT.

2.2.1. PT Thickness

[7] For quantitative analyses, we focus on the Lobbia wavy fault due to better quality field data. The Lobbia wavy fault

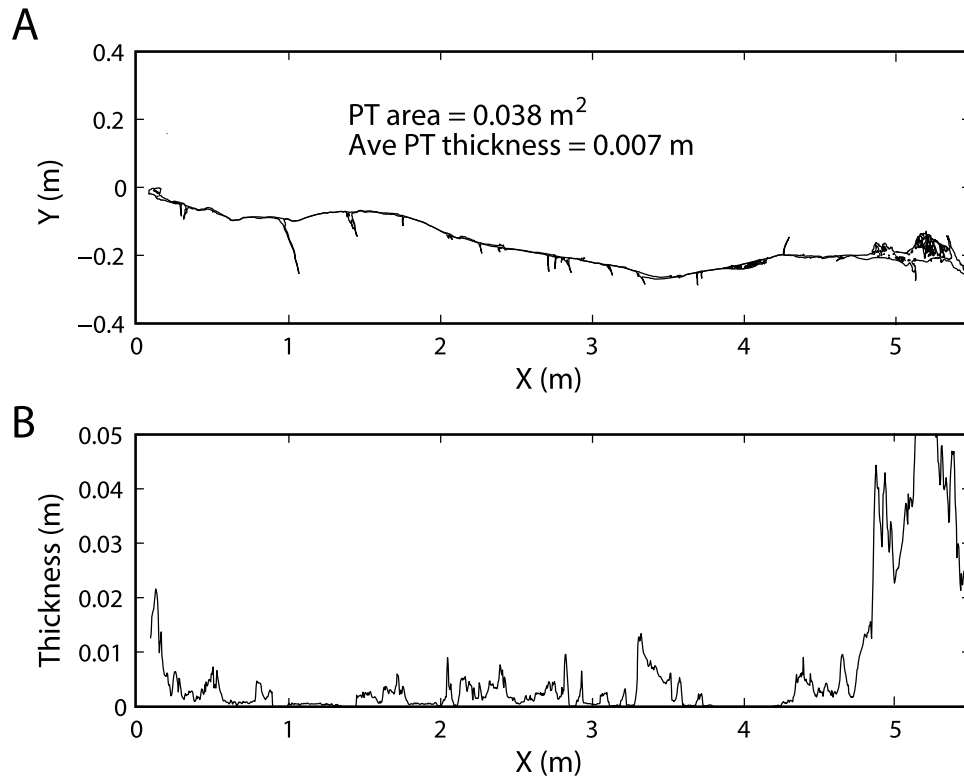


Figure 2. Geometric aspects of pseudotachylyte fault vein from the Lobbia wavy fault. (a) Fault profile used for calculation of pseudotachylyte average thickness. Note vertical exaggeration. (b) Detailed thickness measurements are taken after removal of injection veins. For the purposes of comparing thickness measurements to model opening results in Figure 12, thickness measurements were used only for the first 4.9 m of the full map profile. The fault geometry above 4.9 m as shown in Figure 2a was not included in the model due to the difficulty of approximating the wide reservoir with a single discretized line. See text for further discussion.

structural map was produced using a photomosaic of orthorectified images (Appendix A), whereas the Sierran wavy fault map suffers in precision due to slight optical aberrations in the individual field photos. The exposure of the Lobbia fault was parallel to the net slip vector of the fault as determined by the orientation of slickenlines exposed along the fault. Also, due to the abundance of PT and fresher exposure along the Lobbia wavy fault, the fault profile (i.e., the intersection between the fault surfaces and the outcrop surface) can be constructed with more confidence.

[8] The average thickness of the PT fault vein calculated by measuring the area ($A = 0.038 \text{ m}^2$) occupied by pseudotachylyte along the fault trace is 7.0 mm (Figure 2a). This estimate includes PT in injection veins and will be used as a proxy for coseismic slip in section 3.2.3. Figure 2b shows the thickness profile along the fault and excludes thickness increases around injection veins. This thickness profile will be used in section 4.2.2 as a point of comparison for modeling results.

2.2.2. Roughness

[9] *Dieterich and Smith* [2009] recently showed that for rough, self-similar fault profiles, the roughness can dramatically influence both sliding characteristics and off-fault damage. In that study, the fault profiles were constructed as 2-D surfaces with random fractal roughness, where the mean amplitude of deviations from a locally planar surface were

defined by $h = \beta x^H$, where β is the amplitude factor (rms roughness) and H is the Hurst exponent. The slip deficit relative to a straight fault is directly related to the amplitude factor β . For very large amplitude factors, the slip distribution on a fault deviates significantly from an elliptical profile [*Dieterich and Smith*, 2009, Figure 4]. In addition, for a given roughness, fault slip reaches a maximum value at some fault length above with additional increases in rupture length do not cause an increase in fault slip [*Dieterich and Smith*, 2009, Figure 5]. This maximum normalized slip value d_{\max}' scales with the roughness amplitude as $d_{\max}' = c\beta^{-2}$, where c is a constant that depends empirically on Hurst exponent H . This differs from linear scaling expected between maximum slip and fault dimension for planar crack models, suggesting that, at a given roughness, the slip deficit of a nonplanar fault relative to a planar fault increases nonlinearly as the rupture dimension increases. This relative slip deficit is accompanied by nonuniform stress accumulation in the host rock, the magnitude of which increases linearly with slip.

[10] Qualitatively, the Lobbia wavy fault appears dominated by roughness with wavelength close to the scale of the outcrop exposure (Figure 1b). We computed the roughness of the Lobbia wavy fault from two fault profiles (the northern and southern fault surfaces) taken from the orthorectified outcrop photomosaic as well as profiles of the PT-wall rock contacts mapped on digital scans of thin sections

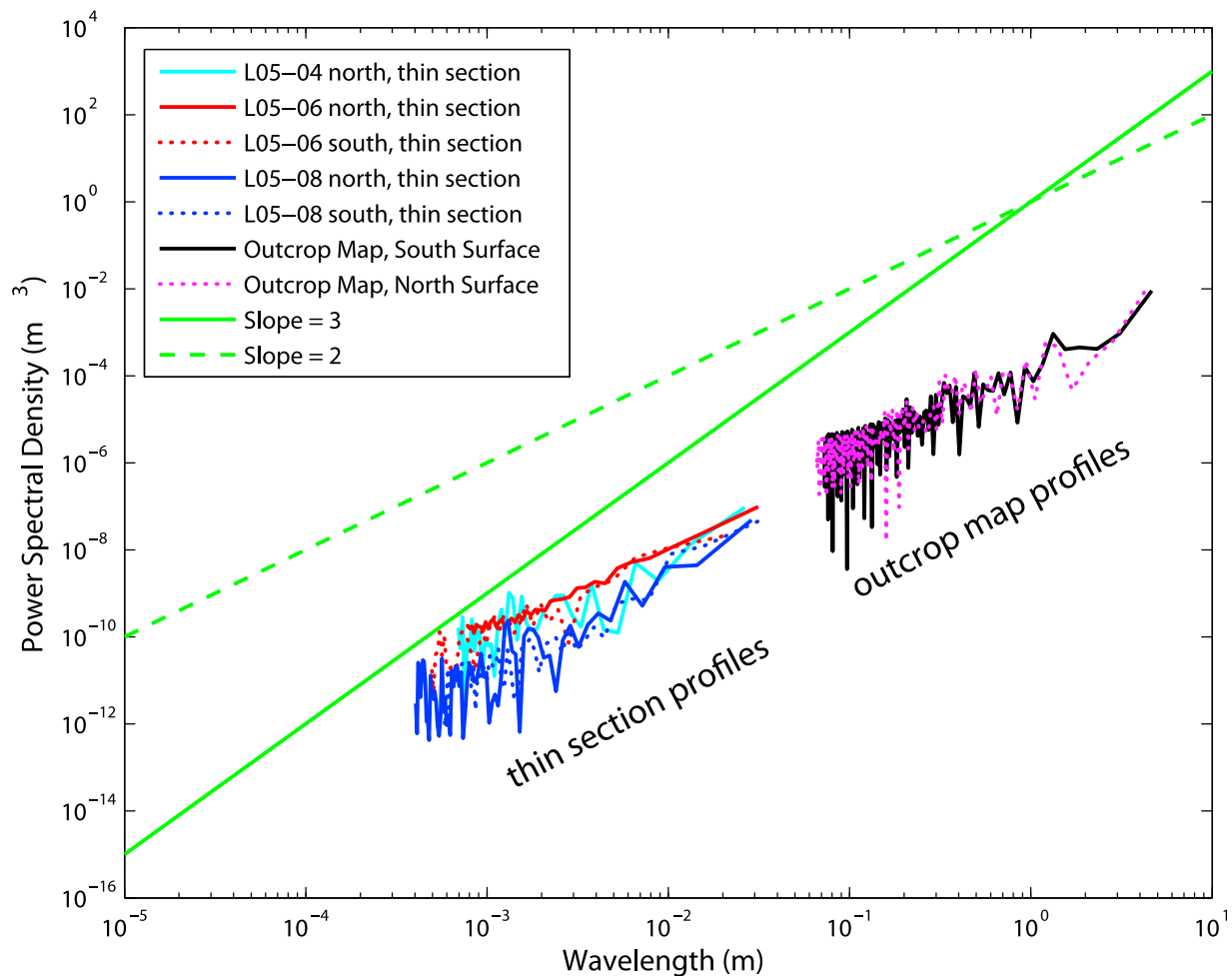


Figure 3. Power spectral density of digitized fault surface profiles. Profiles L05-04, L05-06, and L05-08 are digitized profiles taken from the boundary between PT and wall rock in thin section. The outcrop map profiles are the unfiltered power spectral densities of the northern and southern PT-wall rock boundaries shown in Figure 2a.

(Appendix A). This yielded a power spectrum across over four orders of magnitude (Figure 3). The fault roughness follows power law scaling, as has been reported for slip-parallel profiles on other faults [e.g., *Power et al.*, 1988; *Sagy et al.*, 2007]; however, the slope of the power spectrum is closer to 2 than 3. Locally, between wavelengths of $10^{-3.5}$ and $10^{-2.5}$, this slope is closer to 1. This indicates that the fault is not self-affine, at least at the wavelengths examined. In addition, power at larger wavelengths relative to smaller wavelengths is lower than other reported faults [*Power et al.*, 1987]. Taking the slope α of the power spectrum from the northern and southern outcrop map fault surfaces in Figure 2a, and the relationship $H = -(\alpha + 1)/2$ yields Hurst exponents of $H = 0.4$ and 0.47 , respectively, less than the typical range $0.5 \leq H \leq 1$ expected for self-affine natural fractures [e.g., *Dieterich and Smith*, 2009]. In addition, the roughness amplitude factor β , found by taking the rms slope of the field-scale fault profile, is $\beta \approx 0.1$, placing it in the upper range of the amplitudes examined by *Dieterich and Smith* [2009].

2.2.3. Slip Estimate

[11] A direct measure of slip along the Lobbia wavy fault is not possible, as no offset markers were found along the fault. In lieu of a direct measure, we estimate the slip associated with PT production based on two independent indirect approaches and reach a similar conclusion with both estimates. First, *Di Toro et al.* [2005a] measured the PT thickness and slip along dozens of faults from this outcrop. For faults containing only PT (i.e., no precursory cataclasite), the data plot along a roughly linear trend [*Di Toro et al.*, 2005a, Figure 5]. For an average PT thickness of 7 mm, the value measured for the Lobbia wavy fault (Figure 2a), this trend implies total slip on this fault of less than 100 cm. Because there are no overprinting relationships in the PT veins of the Lobbia wavy fault, we assume that most of the PT thickness was generated in a single event. If this is the case, we may be able to use the length of openings at dilational jogs to approximate slip in a manner similar to *Griffith et al.* [2009a]. The length of the opening at the jog sampled by L05-07 (at 3.3–3.6 m in Figure 1b) is approximately 30 cm. Therefore, we estimate the slip on this fault to be between 30 and 100 cm.

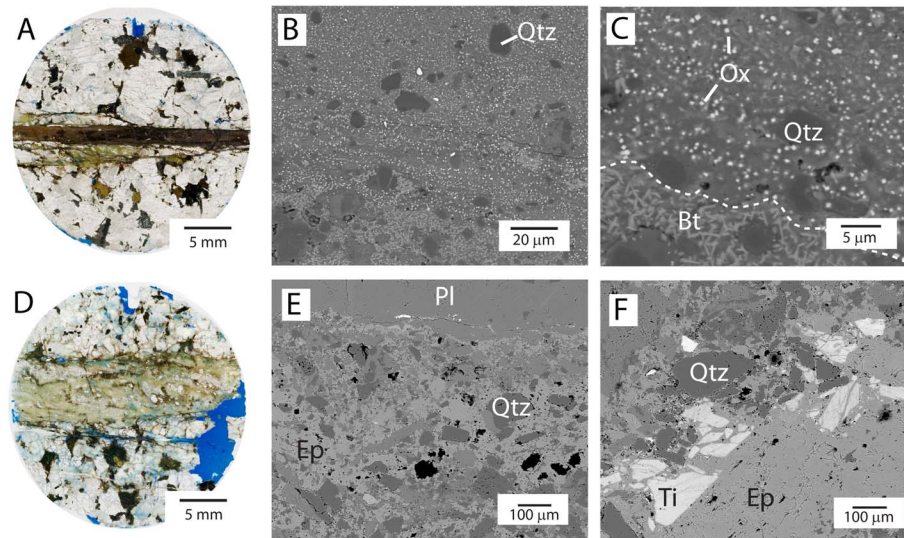


Figure 4. Sierran wavy fault microstructures from contractional (07_118d) and extensional (07_118c) bends (see Figure 1a for sample location). (a) Digital scan of thin section 07-118d, showing dark PT vein and some associated green cataclasite along its boundaries. (b) Backscatter image of heterogeneous PT from sample 07-118d in a contractional bend, showing two textural zones, and dark clasts of quartz (Qtz). (c) Close-up view of the boundary between the compositional zones in Figure 4b. Microlitic domain with biotite (Bt) microlites is below the dashed line, and spherulitic domain with Fe-rich oxides (Ox) is above. (d) Digital scan of thin section 07-118c, showing preexisting quartz mylonite overprinted by green cataclasite. No PT occurs in this sample. (e) Cataclastic fabric consisting primarily of subangular quartz and feldspar grains juxtaposed against a single plagioclase (Pl) grain (top) in the wall rock. Cataclasite is extensively overgrown by epidote (Ep). (f) Epidote matrix in cataclasite with quartz and titanite (Ti) clasts. The titanite (Ti) is extensively fractured and the fractures are filled by epidote veins.

2.3. Microscopic Observations

2.3.1. Fault Rock Descriptions

[12] Microstructures along the Sierran and Lobbia wavy faults were documented using optical and field emissions scanning electron microscopes (FE-SEM). Like other faults described in the area [Griffith *et al.*, 2008, 2009a, 2009b], the Sierran wavy fault consists of a precursory quartz mylonite filling cut by lower-temperature brittle fabrics, including cataclasite and PT veins. Field observations that PT is confined to contractional bends and cataclasites containing hydrothermal minerals are confined to extensional bends are confirmed in thin section [Kirkpatrick and Shipton, 2009]. The PT fault vein in sample 07-118d is approximately 3 mm thick (Figure 4a), forms sharp boundaries with the host rock, and is heterogeneous in composition and texture (Figure 4b). Figure 4b shows two distinct zones within the vein, including a microlitic domain and a spherulitic domain separated by a continuous boundary (Figure 4c). The microlitic domain consists of rounded quartz and plagioclase clasts suspended in a fine-grained matrix made of 5–10 μm long acicular biotite microlites and $\sim 5 \mu\text{m}$ long tabular plagioclase microlites. The spherulitic domain consists of clasts of quartz and plagioclase and spherulites made of feldspar cores rimmed by acicular microlites of plagioclase. Clasts and spherulites are suspended in a cryptocrystalline mica-rich matrix with abundant round Fe oxide blebs, which are interpreted as the result of solidification of Fe oxide-rich immiscible melts, and

minor tabular plagioclase and acicular biotite microlites. In extensional bends, on the contrary, PT is notably absent. Sample 07-118c consists of a quartz mylonite overprinted by a cataclastic material and extensive (green) epidote (Figure 4d). Cataclastic material reflects the host rock composition, with subangular quartz and plagioclase clasts and minor titanite, overgrown by abundant, randomly oriented epidote grains (Figure 4e). A number of clasts are heavily fractured and filled with epidote (Figure 4f). This suggests a cataclastic origin in the presence of abundant fluids.

[13] The Lobbia wavy fault is decorated by PT along its entire length, but the veins are thin in contractional bends and thicken and pool in reservoirs at extensional bends (Figure 1b). At the location of sample L05-06 in a large (~ 1 m) wavelength contractional bend, the average PT thickness is typically less than 100–200 μm (Figures 5a and 5b). Under the optical microscope, the PT consists of rounded to moderately well-rounded clasts of quartz and plagioclase feldspar set among a brown and green cryptocrystalline (fine-grained below microscopic resolution) matrix. Quartz grains in the wall rocks bordering the PT typically display undulose extinction and sets of linear fluid inclusion trails, interpreted as remnants of healed microcracks. In the FE-SEM (resolution, 4 nm) equipped with the backscattered electron (BSE) detector (resolution, 400 nm [Del Gaudio *et al.*, 2009]), quartz grains in the PT matrix (and sometimes in the wall rocks at the contact with the PT) commonly display a very fine subgrain

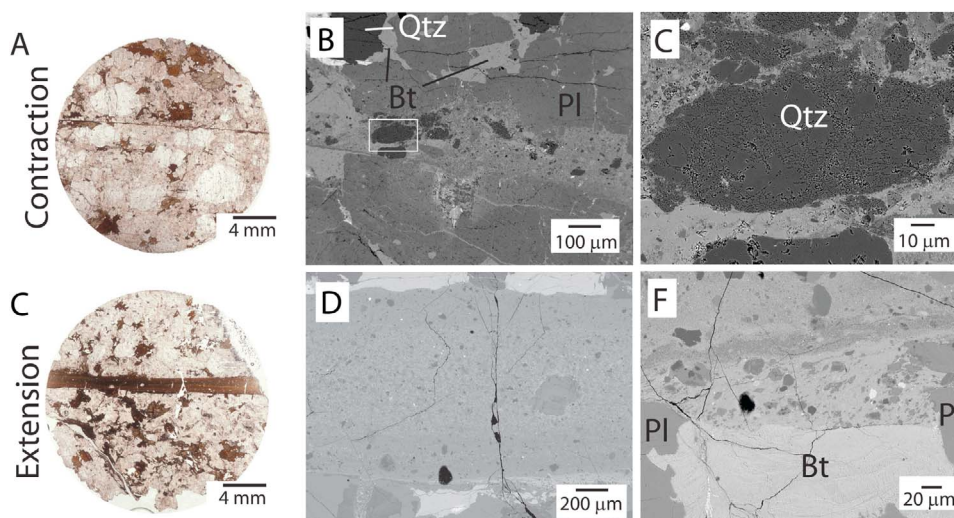


Figure 5. Lobbia wavy fault microstructures from contractional (L05-06) and extensional (L05-08) bends (see Figure 1b for sample location). PT in the Lobbia fault is found in both extensional and contractional bends. (a) Fault thickness in contractional domains is typically less than 100–200 microns, and (b) the PT-wall rock boundaries are typically straight on one side of the fault and very rough on the other. (c) In contractional domains, quartz grains with unique subgrain textures are common. (d) In extensional domains, fault thickness is typically several hundred microns to several millimeters. (e) Survivor clasts of host rock are suspended in the PT cryptocrystalline matrix. Note PT injection vein in lower left corner of image. (f) Roughness on the PT-wall rock boundaries is enhanced by preferential melting between biotite (Bt, melting point $\sim 700^{\circ}\text{C}$) and adjacent quartz (Qtz, melting point $\sim 1700^{\circ}\text{C}$) and plagioclase feldspar (Pl, melting point $\sim 1200^{\circ}\text{C}$).

microstructure, consisting of euhedral to subangular nanometer to micrometer quartz grains immersed in a cryptocrystalline material below the 4 nm resolution of the FE-SEM made of silica, aluminum, and calcium (semiquantitative energy dispersive spectroscopy) (Figure 5c). The boundary between PT and wall rocks is typically straight and sharp on one side of the fault vein and rough on the other side; however, the smooth and rough boundaries do not appear to remain on one side of the fault consistently. In sample L05-08 (Figure 5d), in a large wavelength extensional bend, the average thickness of the PT fault vein is approximately 2 mm. Both borders in this sample are sharply defined with occasional injection veins (Figure 5e), and along both borders, densely kinked biotite grains are typically embayed, presumably due to preferential melting of biotite (Figure 5f). In thicker reservoirs, such as that sampled in L05-07, thin chilled margins and flow structures are present and multiple layers of PT are preserved (Figure 6). Figure 6a is a photomosaic transect across the reservoir at the center of sample L05-07 (Figure 6b) and shows several alternating layers defined by microstructural and mineralogical changes seen under backscatter electron SEM images. These layers are dominated either by spherulites nucleated by survivor quartz or plagioclase grains (Figure 6c) or biotite and potassium feldspar microlites (Figures 6c and 6d). Frequently, these $\sim 10\text{--}50\text{ }\mu\text{m}$ thick layers are folded together (Figures 6b and 6c), suggesting that they coexisted as immiscible melts. We interpret these layers to represent multiple pulses of melt of different composition and temperature injected into the reservoir during the same slip event from different locations along the fault [e.g., Warr *et al.*, 2003]. This interpretation implies that melt was generated heterogeneously along the

fault (likely preferentially in contractional domains) and transported along the fault.

2.3.2. Quartz Microcracks

[14] In the host rock, microcracks are pervasive along the Lobbia wavy fault: biotite and feldspar grains are typically fractured along cleavage planes, while quartz grains preserve healed fractures in the form of subplanar fluid inclusion trails. Qualitatively, quartz microcracks appear to form in moderately well-defined sets, and any given quartz grain may preserve between one (Figures 7a, 7c, and 7e) to three (Figures 7b, 7d, and 7f) main fracture sets. In some samples, quartz microcracks appear as discrete surfaces, while in others fractures are healed by fluid inclusion trails (Figure 7). In some samples, particularly in extensional domains (e.g., L05-03, L05-07), intragranular microcracks are accompanied by significant intergranular cracking dominantly oriented subparallel to the local fault strike (Figure 7b). In section 3.3.3, we report measured spatial variations in microcrack orientation and density in quartz grains.

2.3.3. Microcrack Distribution

[15] We used thin sections drilled along the Lobbia fault and cut parallel to the slip direction to study spatial patterns of quartz microcrack orientation and density (Appendix A). Microcracks were measured in at least two quartz grains in each sample, and each rose diagram in Figure 8 represents the cumulative orientation data for each sample. Because samples L05-04, L05-06, and L05-07 cross the fault and preserve fractured quartz grains from both the northern and southern sides of the wall rock, data from samples are divided into northern and southern rose diagrams for each sample. Looking at the data in Figure 8, some systematic variations in microcrack orientation with the local strike of the fault are

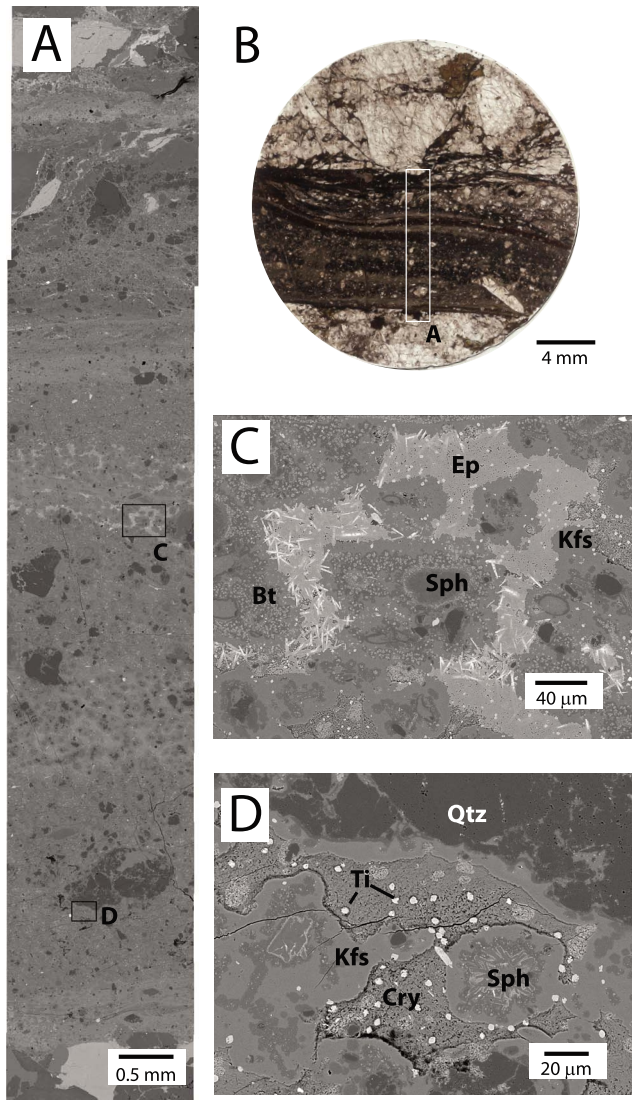


Figure 6. Lobbia wavy fault microstructures from PT reservoir (L05-07) (see Figure 1b for sample location). (a) A photomosaic transect across the pseudotachylyte reservoir shown in Figure 6b, documenting the compositional and textural changes between different layers. (c) Spherulites (Sph) suspended in a folded, multilayered matrix, which is composed of K-feldspar (Kfs, medium-gray homogeneous layers), biotite-rich microcrystalline layers (Bt, darker in color relative to Kfs), and Epidote-rich layers (Ep, lightest in color, possibly due to later pseudomorphic overgrowth of pseudotachylyte). (d) Spherulites suspended in homogeneous K-feldspar (Kfs) and in a cryptocrystalline (Cry) matrix of plagioclase and biotite. Bright spots (Ti) are titanite/biotite clusters [e.g., Di Toro and Pennacchioni, 2004].

evident. First, in the large contractional bend of the fault (samples L05-05, L05-06, and L05-11), there is a single predominant fracture set oriented at high angles to the fault. Immediately adjacent to the fault in L05-06, this fracture set is precisely orthogonal to the fault. A few centimeters away from the fault in this location, the spread of orientation data is slightly larger, and the principal orientation of the fractures makes a $\sim 80^\circ$ angle with the local fault strike. Second, in all

extensional domains of the fault (samples L05-02, L05-03, L05-07, L05-09, L05-10), there are at least two prominent microcrack sets, with one set subparallel to the fault. In several samples, namely L05-03 and L05-07, this microcrack set is accompanied by a pervasive set of subparallel intergranular fractures, which are filled variably with pseudotachylyte and comminuted material. We deem the location of samples L05-04 and L05-12 to be a “transitional” zone, because even though the local fault strike suggests that it should be a contractional bend in the current fault configuration, the fault strike changes considerably to an extensional orientation within several centimeters.

[16] The measured fracture densities (Appendix A) are shown in Figure 8 in the lower inset box on each rose diagram, along with the number of segments. Like fracture orientation, microcrack density varies along the fault, systematically with the local strike of the fault, with higher fracture densities corresponding to extensional sections of the fault, and lower densities corresponding to contractional zones of the fault (Figure 8). Like the orientation data, the microcrack densities seem to be consistent north and south of the fault, even though they vary systematically along the fault strike.

3. Modeling of Frictional Slip on Nonplanar Faults

[17] The purpose of modeling in the current study is threefold, including (1) to estimate the effect of fault waviness on slip resistance, (2) to investigate the role of slip in off-fault yielding on wavy faults, and (3) to estimate the variability of fault-normal tractions on the fault due to waviness. Below we discuss the creation of the fault mesh, the numerical method, selection of boundary conditions, and then the results.

3.1. Model

[18] We model slip and deformation on the wavy Lobbia fault using a 2-D boundary element displacement discontinuity method (BEM) introduced by Crouch [1976], which treats the fault as curvilinear boundary discretized into elements (constant displacement discontinuities) and embedded into an infinite medium (Figure 9). While three dimensionality of fault roughness is certainly an important mechanical aspect of fault slip [e.g., Sagy et al., 2007; Sagy and Brodsky, 2009; Resor and Meer, 2009], our choice of a 2-D modeling technique is most appropriate given the geometrical constraints afforded by our field observations. This method has the advantage that the geometry of any irregular surface(s) can be represented in the model given that the elements are small enough [e.g., Cooke and Kameda, 2002; Dieterich and Smith, 2009]. Quasi-static deformation in an infinite whole space is driven by a remote stress tensor. The stresses and displacements throughout the body can be calculated uniquely given boundary conditions on the discontinuities (Figure 9). One of the most difficult parts of dealing with frictional contact on the discontinuities, however, is that in the presence of geometric irregularities or multiple fractures, the boundary conditions on the fracture are not known a priori and are impossible even to estimate by intuition. The contact problems on the discontinuities are instead solved using a complementarity algorithm implemented in Matlab by O. Mutlu [Mutlu and Pollard, 2008].

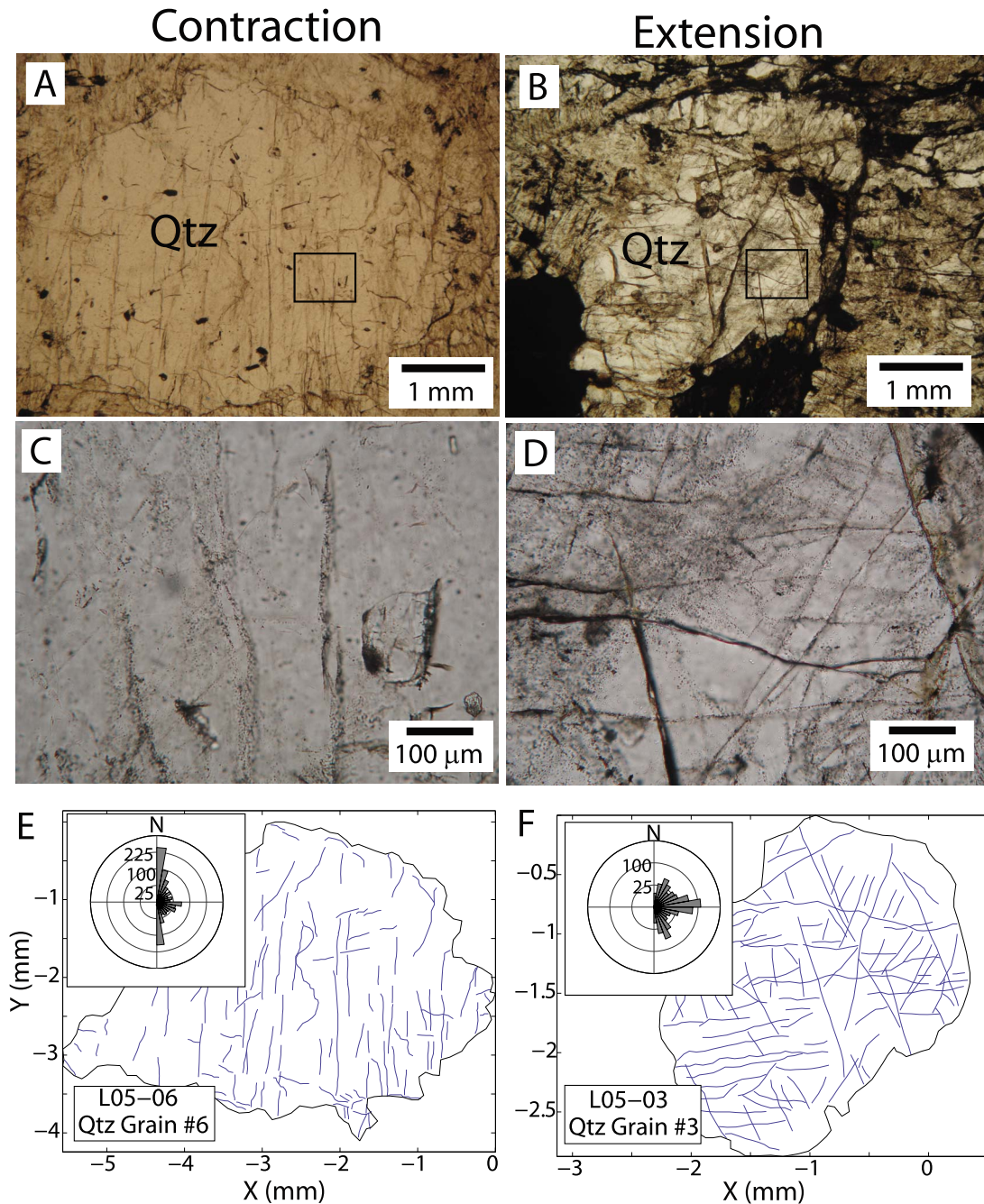


Figure 7. Plane polarized light photomicrographs of microcracks in quartz grains from (a, c) contractional and (b, d) extensional domains of the Lobbia wavy fault (see Figure 1b for sample location). In all figures, north is up. (a) Quartz grain from sample L05-06 showing microcracks dominantly oriented north–south, orthogonal to the local fault strike (roughly east–west; see Figure 1b). (b) Quartz grain from sample L05-03 showing several sets of microcracks healed by fluid inclusion trails. (c) Close-up view of black box in Figure 7a, showing prominent north–south trending microcracks. (d) Close-up view of black box in Figure 7b showing three distinct sets of microcracks, trending roughly east–west, northeast–southwest, and north northwest–south southeast. In the northwest corner of the image, several microcracks have coalesced, such that it is difficult to discriminate between fractures. This increase in microcrack density relative to the quartz grain shown in Figures 7a and 7c is typical of extensional domains. (e, f) Digital maps used to measure microcrack orientation and density and resulting rose diagram (inset) for the quartz grains pictured in Figures 7a and 7b, respectively. See description of method in the text.

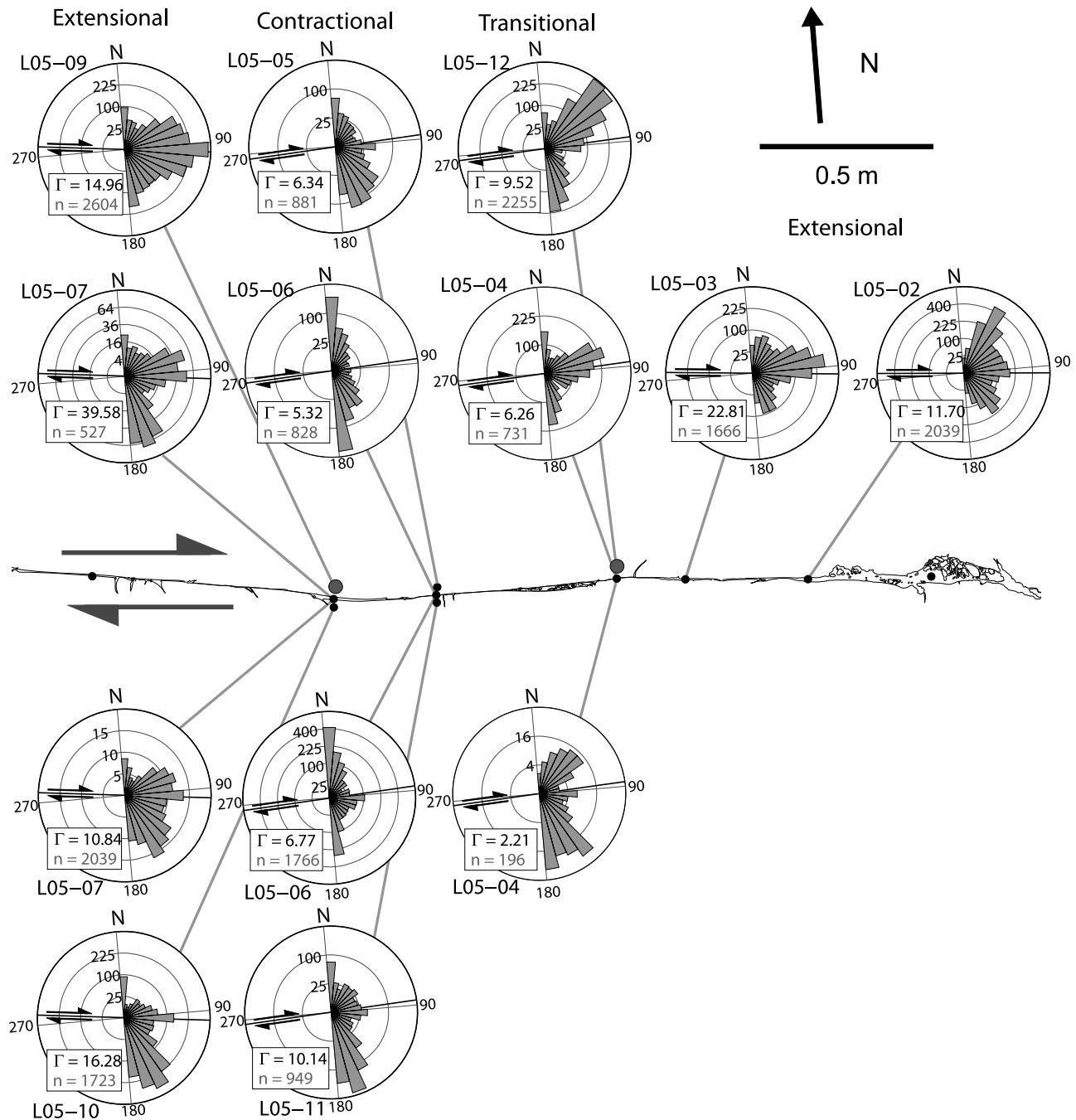


Figure 8. Measurements of microcrack orientation and density for samples L05-02, L05-03, L05-04, L05-05, L05-06, L05-07, L05-09, L05-10, L05-11, and L05-12. Note that sample L05-08 was not used because no suitable quartz grains could be found in the thin section. Rose diagrams are scaled to the square root of the measurement frequency, so areas in the diagrams are proportional to frequency. Local fault orientation is indicated in each of the rose diagrams.

The applicability of the “complementarity” algorithm to fracture problems stems from the complementary nature of the normal traction and relative displacement across a fracture: if the normal displacement discontinuity on a fracture element is nonzero (i.e., it is open), the normal traction must be zero, and vice versa [e.g., *De Bremaecker et al.*, 2000]. The algorithm uses six inequality constraints which prevent interpenetration, enforce a Coulomb sliding criterion, and allow for relative opening displacements. The application of

complementarity to the displacement discontinuity method is discussed in greater detail by *De Bremaecker et al.* [2000] and *Mutlu and Pollard* [2008]. This approach has advantages over other contact algorithms such as the penalty method and Lagrange multipliers because it avoids artificial regularization parameters and is numerically efficient [e.g., *Mijar and Arora*, 2000; *De Bremaecker and Ferris*, 2004; *Mutlu and Pollard*, 2008]. The complementarity approach also offers significant advantages over other numerical and analytical

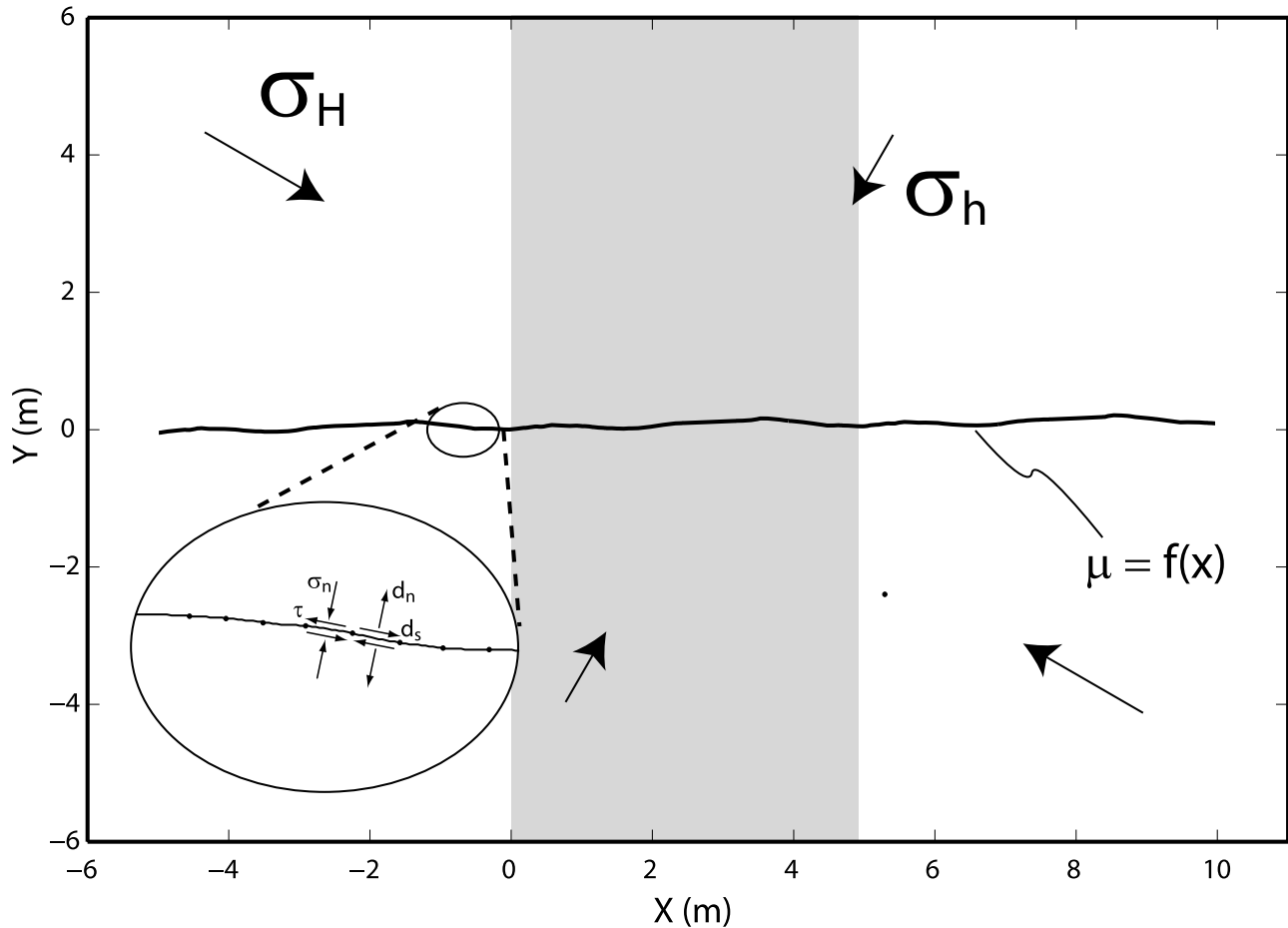


Figure 9. Model boundary setup. The model fault is composed of 1505 constant displacement discontinuity elements embedded into an isotropic, homogeneous infinite whole space, and plane strain is assumed. The fault profile produced from the field map corresponds to the central profile (gray) between $x = 0$ and 5 m. Periodic boundary conditions at the ends of the mapped fault profile are produced by placing identical fault profiles at either end of the central profile. This moves the tip affects far from the central, mapped fault profile. Each element is assigned a coefficient of friction. Traction and displacements are calculated at the center of each element (inset) in response to an imposed remote stress tensor, illustrated by arrows labeled σ_H and σ_h . Note that the sign convention used for tractions and displacements are illustrated in the inset: each traction and displacement component is shown in the positive sense. For further details, see also Appendix B.

studies on the effects of waviness on fault slip because it takes frictional effects into account [e.g., *Saucier et al.*, 1992], allows for opening displacements along the fault elements [e.g., *Nielsen and Knopoff*, 1998; *Chester and Chester*, 2000; *Dieterich and Smith*, 2009], and makes no assumptions regarding the magnitude of changes in local strike along the fault [e.g., *Chester and Chester*, 2000]. To our knowledge, the complementarity algorithm has not been used to model slip on faults with significant roughness; therefore, we confirmed its performance by reproducing photoelastic fringe patterns produced during uniaxial experiments in CR39 Columbia Resin (Appendix B).

[19] We use geological field observations to specify necessary geometrical and boundary conditions for the model. Because the fault tips were not exposed in the field, we use other information to infer fault length for our simulations. Individual fault strands in the Lobbia can be tens to hundreds of meters in length, and the effective length of an individual

fault strand can be several kilometers due to fault linkage [*Di Toro and Pennacchioni*, 2005] and have total slip from several millimeters to tens of meters (the latter is cumulative slip accommodated by the fault and includes several seismic ruptures). Clearly, constraining exact single-jerk source parameters for either fault is difficult. Instead, we work with boundary conditions that can be constrained from field observations. We assume that the fault exposure we mapped is at least several meters away from a fault tip. To do this, we extend the fault to three times its mapped length by attaching three identical fault profiles end to end, in effect creating a single periodic fault profile (Figure 9). This is, in effect, applying periodic boundary conditions to the end elements of the central fault profile. Deformation on the fault is driven by a geologically constrained remote stress tensor following *Di Toro et al.* [2005a] and used by *Di Toro et al.* [2005b] as the static background stress for dynamic rupture simulations. We assume that the stress field is Andersonian hydrostatic

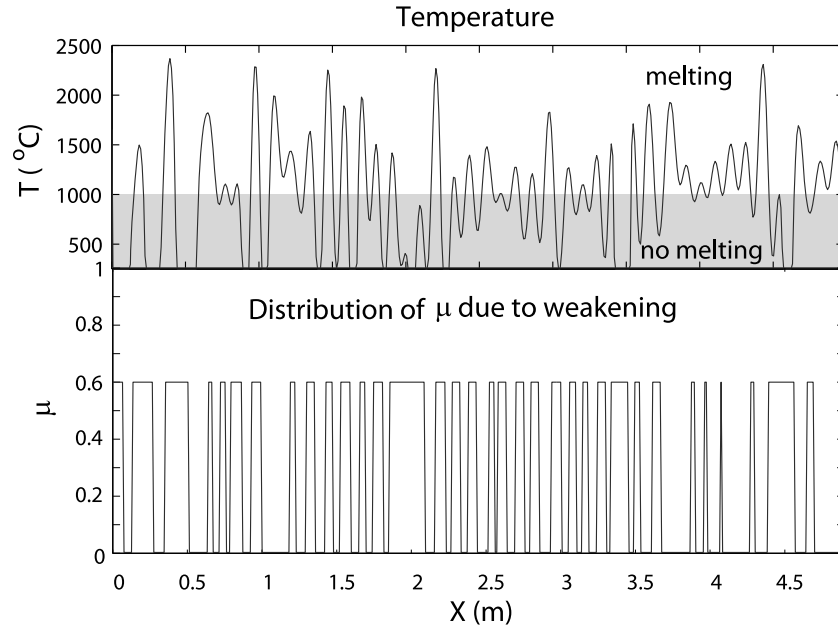


Figure 10. (top) Temperature rise and (bottom) resulting heterogeneous friction distribution due to slip on a model fault with uniformly high friction ($\mu = 0.6$). Elements in which temperatures surpass 1000°C are assigned for the subsequent simulation, assuming that the amount of time that it would take for melting to initiate is much smaller than the total time of slip. See text for complete discussion.

(i.e., the pore fluid factor, $\lambda = 0.4$), the depth of burial is $z = 10,000$ m, acceleration due to gravity is $g = 10 \text{ m s}^{-2}$, static coefficient of friction is $\mu = 0.75$, and $\rho = 2650 \text{ kg m}^{-3}$. In this case, the optimal angle θ between the fault (here taken as the mean orientation of the fault) and the maximum principal stress direction is $\theta = 1/2 \tan^{-1}(1/\mu_s) \approx 26.5^{\circ}$; the ratio between principal stresses, $R = \sigma_H/\sigma_h$, is given by $R = [\sin 2\theta + \mu_s (\cos 2\theta + 1)]/[\sin 2\theta + \mu_s (\cos 2\theta - 1)]$ [e.g., *Sibson, 1974*]. Given these assumptions, $R = 4$. The assumption that the effective vertical stress (also the intermediate principal stress) is $\sigma_v = \rho g z (1 - \lambda)$, yields $\sigma_H = 254 \text{ MPa}$ and $\sigma_h = 64 \text{ MPa}$. Also, because the model assumes small strains, we are not able to model the total slip of a single slip event, if the estimate of 30–100 cm is correct. Because the model preserves waviness at wavelengths as small as 10 cm, slip on the order of 30–100 cm would result in significant alteration of the fault geometry, particularly at wavelengths on the order of the slip. Therefore, we confine our study to small slips (< 7 cm) and focus on the mechanical relationship between fault roughness, tractions, and slip at small displacements less than the dimension of the smallest geometrical irregularities. In this way, we are interested in matching general patterns of deformation observed along the fault instead of trying to match field observations absolutely.

[20] We assume for a starting case that the friction coefficient is constant along the length of the fault. As upper and lower bounds for fault friction, we calculate deformation on a lubricated ($\mu = 0$) fault and a fault subject to a higher friction coefficient ($\mu = 0.6$). For comparison, we also run simulations for a straight fault parallel to the least squares best fit of the wavy fault with constant friction $\mu = 0$ and $\mu = 0.6$. Because it is well established that frictional resistance varies during slip due to a number of mechanisms (i.e., flash heating [Rice, 2006], melt lubrication [Nielsen et al., 2008], thermal

pressurization [Lachenbruch, 1980], acoustic fluidization [Melosh, 1996], elastohydrodynamic lubrication [Brodsky and Kanamori, 2001], etc.), we also attempt to approximate fault weakening processes during slip in two ways.

[21] In the first case, we assume that the primary weakening mechanism was melting. We calculate the temperature rise associated with slip and normal tractions associated with an event with ($\mu = 0.6$) using the approximation [Carslaw and Jaeger, 1959] $T_{\max} = T_{\text{amb}} + \mu \sigma_n d / \rho c_p \sqrt{\pi \kappa t^*}$, where T_{amb} is the ambient temperature taken to be 250°C [Di Toro and Pennacchioni, 2004], μ , σ_n , and d (slip) are calculated uniquely for each element, density ρ is 2650 kg m^{-3} , specific heat c_p is taken to be $1200 \text{ J kg}^{-1} \text{ K}^{-1}$ [Di Toro and Pennacchioni, 2004], and thermal diffusivity κ is taken to be $0.86 \times 10^{-7} \text{ m}^2 \text{ s}^{-1}$. Note that in this case, the choice of $\mu = 0.6$ instead of 0.75 reflects the need for the entire fault to be slipping before sufficient slip to cause melting can occur. Time of slip $t^* = v/d$ is calculated on each element from d assuming average slip velocity $v = 1 \text{ m s}^{-1}$ (average slip rate during seismic slip [Heaton, 1990]). For a first-order estimate of the initial distribution of melt along a fault of the given geometry and loading conditions, we assume that any element with a maximum temperature $T_{\max} > 1000^{\circ}\text{C}$ experiences melting and a drop of sliding friction to $\mu = 0$. Elements on which the temperature does not reach this threshold are assumed to maintain the original friction coefficient $\mu = 0.6$ (Figure 10). We then rerun the slip simulation with the heterogeneous friction distribution but the same remote stress tensor. The slip results are plotted in Figure 11.

[22] For the second case, we adopt a more natural simple weakening criterion similar to that simplified slip-weakening implemented by Nielsen and Knopoff [1998]. The stress tensor used in the preceding simulations is designed to criti-

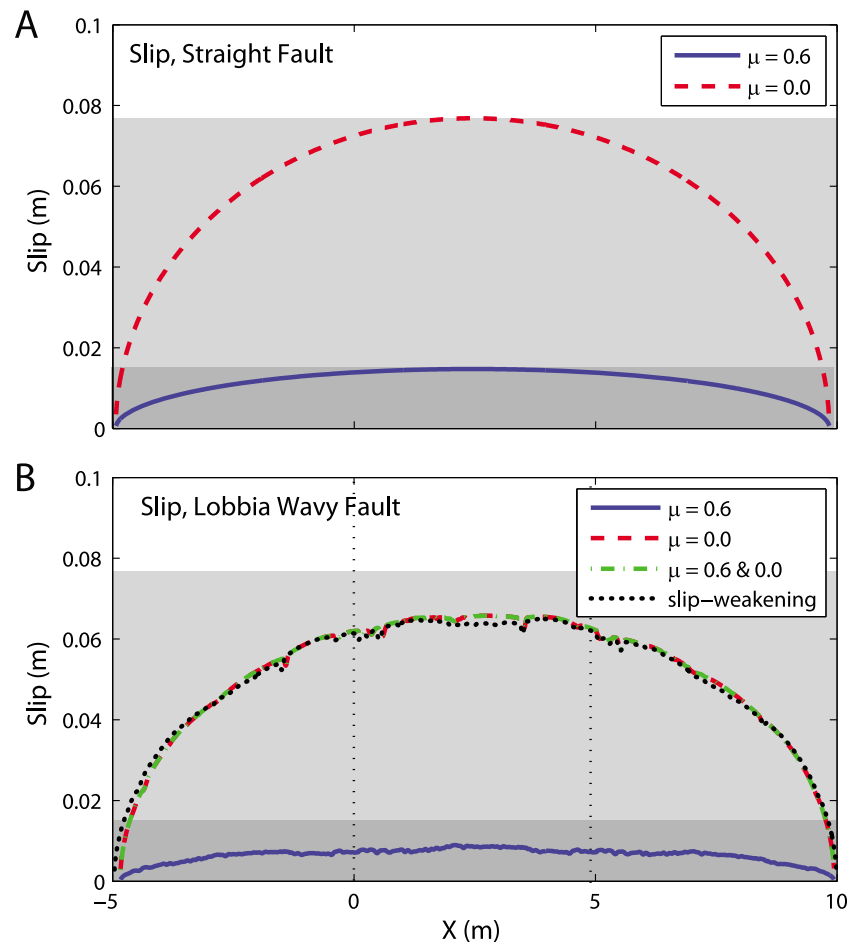


Figure 11. Modeled slip distributions for different frictional cases on a (top) straight and (bottom) wavy fault. According to our model, only in the case for a constant and high ($\mu = 0.6$, blue line) friction coefficient, the displacement accommodated during seismic slip in the straight fault is much higher than in the wavy fault. For lubricated fault models (coefficient of friction at or near zero), the slip deficit relative to the straight fault is very small.

cally stress a straight incohesive fault with a static coefficient of friction $\mu = 0.75$ oriented at an optimal angle for reactivation. However, because the modeled Lobbia wavy fault is composed of over 1500 elements of length < 1 cm at orientations less than, equal to, and greater than the critical angle for Coulomb failure, only a few of the elements would slip given uniform friction $\mu = 0.75$ across the entire fault. For this case, we use an iterative approach to calculate deformation along the fault. Starting with a uniform friction $\mu = 0.748$, we subject the fault to the same far-field loading as in the other simulations and calculate the equilibrium traction and slip distribution along the faults. If an element slips, friction is dropped to $\mu = 0$ on the corresponding element and remains elsewhere $\mu = 0.748$. In addition, fault elements are allowed to open. In the case of opening, as in the other simulations described here, the effective coefficient of friction is zero. In the next iteration, the equilibrium traction distribution calculated in the preceding iteration drives slip on the fault, and so on, until the shear traction has been relieved on all of the elements, or until no more elements are brought to failure. The final fault-parallel displacement distribution resulting from this simulation is plotted along with other simulations in Figure 11. Opening distributions are plotted in Figure 12.

3.2. Model Results

3.2.1. Slip Distribution

[23] Simulations for the straight fault show the elliptical slip profile with uniform stress drop and constant frictional resistance (Figure 11). Peak slip for the straight fault with constant $\mu = 0.6$ is 15 mm and 77 mm for $\mu = 0.0$ (Table 1). Maximum slip for the straight fault cases are highlighted with gray boxes in Figure 11 for comparison with simulations with the wavy fault geometry. As expected, slip distributions for the wavy fault are nonelliptical, and peak slip is less in each case than the straight fault with corresponding frictional resistance. Notable is the fact that all three lubricated fault models, (1) $\mu = 0.0 = \text{constant}$; (2) $\mu = 0.0$ in melted patches and $\mu = 0.6$ in unmelted patches; (3) and the slip weakening model, produce roughly the same final slip distribution as for the straight fault. Peak and average values are slightly lower for the slip weakening model but negligibly so considering the uncertainties regarding the starting fault geometry and unaccounted- for three-dimensional effects. Also notable is the fact that the slip weakening model achieves complete stress drop after only four iterations. This is likely due to enhanced weakening in extensional bends due to opening: as

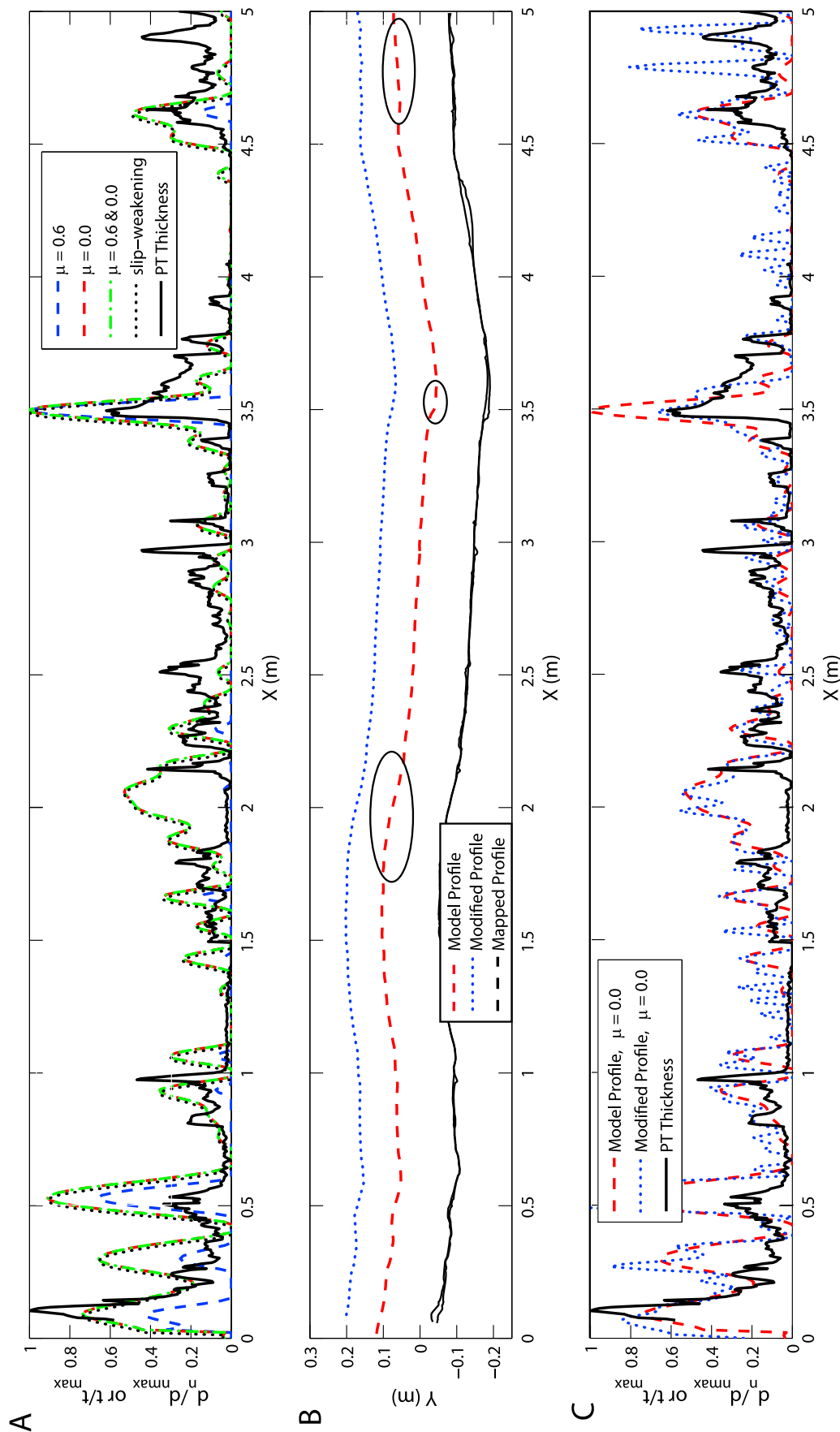


Figure 12. (a) Comparison of model opening distributions for each wavy fault simulation compared to the PT thickness measurements. (b) The fault geometry is the same for each simulation. Each opening profile is normalized by the maximum observed value (d_{\max} or t_{\max}) of opening (d_n) or PT thickness (t) for each case. Only opening distributions along the central section ($0 \text{ m} < x < 5 \text{ m}$) of each modeled fault are shown for comparison purposes. The model profile is an approximation of the mapped profile. This approximation is necessary because the fault is represented as a curved, discretized line in the model. The model geometry was altered slightly (ellipses, Figure 12b) at locations of poor model fit, and the resulting slip is plotted in Figure 12c.

Table 1. Variables for and Results of Simulations

Fault Geometry	Friction	Max Slip (mm)	Mean Slip (mm)	Max Opening (mm)	Mean Opening (mm)	Slip Deficit (%)
Straight	$\mu = 0.0$, constant	77	60	0	0	-
Straight	$\mu = 0.6$, constant	15	12	0	0	-
Wavy	$\mu = 0.0$, constant	66	52	18	2	13
Wavy	$\mu = 0.6$, constant	9	6.5	1.4	0.4	46
Wavy	$\mu = 0.6 \rightarrow 0.0$, heterogeneous	66	52	18	2	13
Wavy	$\mu = 0.75 \rightarrow 0.0$, weakening	65	51	18	2	15

elements favorably oriented for slip weaken and slip, elements in extensional zones of the fault begin to open and slip without undergoing any slip-weakening transition (i.e., drop in friction coefficient).

[24] We compare the slip results for the wavy fault simulations to the reference straight fault simulations by calculating the slip deficit defined by $(\bar{d}_{\text{straight}} - \bar{d}_{\text{way}})/\bar{d}_{\text{straight}} \times 100$ where the overbar denotes the arithmetic mean value. For lubricated wavy faults, mean slip is only 13%–15% less than along the corresponding straight fault, whereas for the unlubricated wavy fault, the slip deficit is 46% relative to the straight fault. This difference in slip deficit highlights the role of fault opening in enhancing fault weakening. Increased slip for the lubricated fault cases results in greater fault opening in extensional domains, domains which would be less likely to undergo weakening due to thermal processes (thermal pressurization, melting, etc.). This opening results in an effective drop in the local friction coefficient to zero, resulting in a more homogeneously weak fault.

3.2.2. Opening Distribution

[25] Because the slip distribution cannot be directly measured in the field, we compare the modeled opening distribution to the fault thickness measured in the field. Figure 12a shows the distribution of opening calculated for wavy fault geometries with different models of frictional resistance. The opening is normalized by the maximum opening value because the absolute values vary significantly (as expected) between the various models and the field example, as we do not attempt to simulate the large finite deformation. Because the modeled fault consists of three identical fault profiles placed end to end, only the central section of the modeled fault is compared to the field thickness distribution here. Note that zero opening occurs along the straight fault, so these results are omitted from Figure 12. In a similar fashion to the results for slip, all three lubricated models produce roughly the same opening distribution, while significantly less opening occurs for the high friction simulation. In comparison to the thickness profile from the field data, two things are immediately clear. First, the opening distribution (Figure 12a) at the tips of the model fault profile does not correspond well to the thickness distribution. This is not surprising both because of the uncertainty in dealing with the boundary conditions at the ends of the mapped fault profile (see section 4.1) and also because the initial geometry of the fault in the large PT reservoir from 0 to 0.25 m on the profile is difficult to constrain. Second, the opening at positions 2, 3.5, and 4.5 m are significantly overpredicted in the model. This is likely to do with the choices made in creating the fault profile. Because the fault, which has significant PT thickness changes along strike, needs to be represented as a curved line in the model, the modeled slope of the initial fault surface may be more steep (encouraging opening) than

that of the starting natural fault configuration at those locations. Indeed, slight changes to the model fault profile at 3.5 and 4.6–5 m (modified profile in Figure 12b) improve the match between the model opening and PT thickness profiles considerably, even though the section between 0 and 0.4 m is the end of the mapped profile (Figure 12c); however, the fit is still poor at 2 m after slight alterations to the geometry, because the thinness of the mapped fault at that location limits the amount that the model geometry can be altered. Nonetheless, the lubricated fault models show good agreement with the thickness profiles at several wavelengths, particularly in light of the fact that (1) the model is two dimensional and (2) the path of deformation along the fault from initial to final configurations is ambiguous and likely not adequately represented by a single static geometry.

3.2.3. Static Stress Distribution Around Faults

[26] Because the slip distribution was largely indistinguishable for all three lubricated fault cases, the resulting stress distribution solutions are very similar. Therefore, we only discuss the stress distribution around the most simple lubricated ($\mu = 0$) wavy fault case, and it is implicit that this is representative of all lubricated fault cases. Figure 13 shows the maximum compressive stress and minimum compressive stress distributions due to slip on (1) a high friction ($\mu = 0.6$) wavy fault compared to a high friction ($\mu = 0.6$) straight fault and (2) a lubricated ($\mu = 0$) wavy fault compared to a lubricated ($\mu = 0$) straight fault. Several observations are of note.

[27] Stress varies significantly in both its distribution and magnitude for the wavy fault model depending on the friction model used (Figure 13). First, for the high-friction (i.e., small slip) case on the wavy fault, smaller wavelength roughness of the fault surface dominates the distribution of both principal stress components. Lobes defined by the stress contours, emanating from the model fault surface, are of the same width as the smallest wavelengths preserved in the fault mesh (10–20 cm). For the lubricated case (i.e., larger slip) on the wavy fault, small fluctuations in stress persist along strike; however, the larger wavelength roughness of the wavy fault surface become important as evidenced by wider stress contours (1–2 m). Instead, no significant variation occurs in the stress patterns around the central portion of straight fault for either friction model. In both cases, the minimum value observed for the minimum compressive stress is zero. These local minima are locations where opening occurred along the fault in the models (Figure 12). As with the case of stress pattern, the magnitude observed along the center section of the model fault does not change significantly. This is because for the case of the straight fault, deformation is predicted to be concentrated near the fault tips (not pictured in Figure 13).

[28] A major difference between unlubricated and lubricated wavy faults is the degree of stress rotation induced along the fault. For the case of unlubricated faults, like the

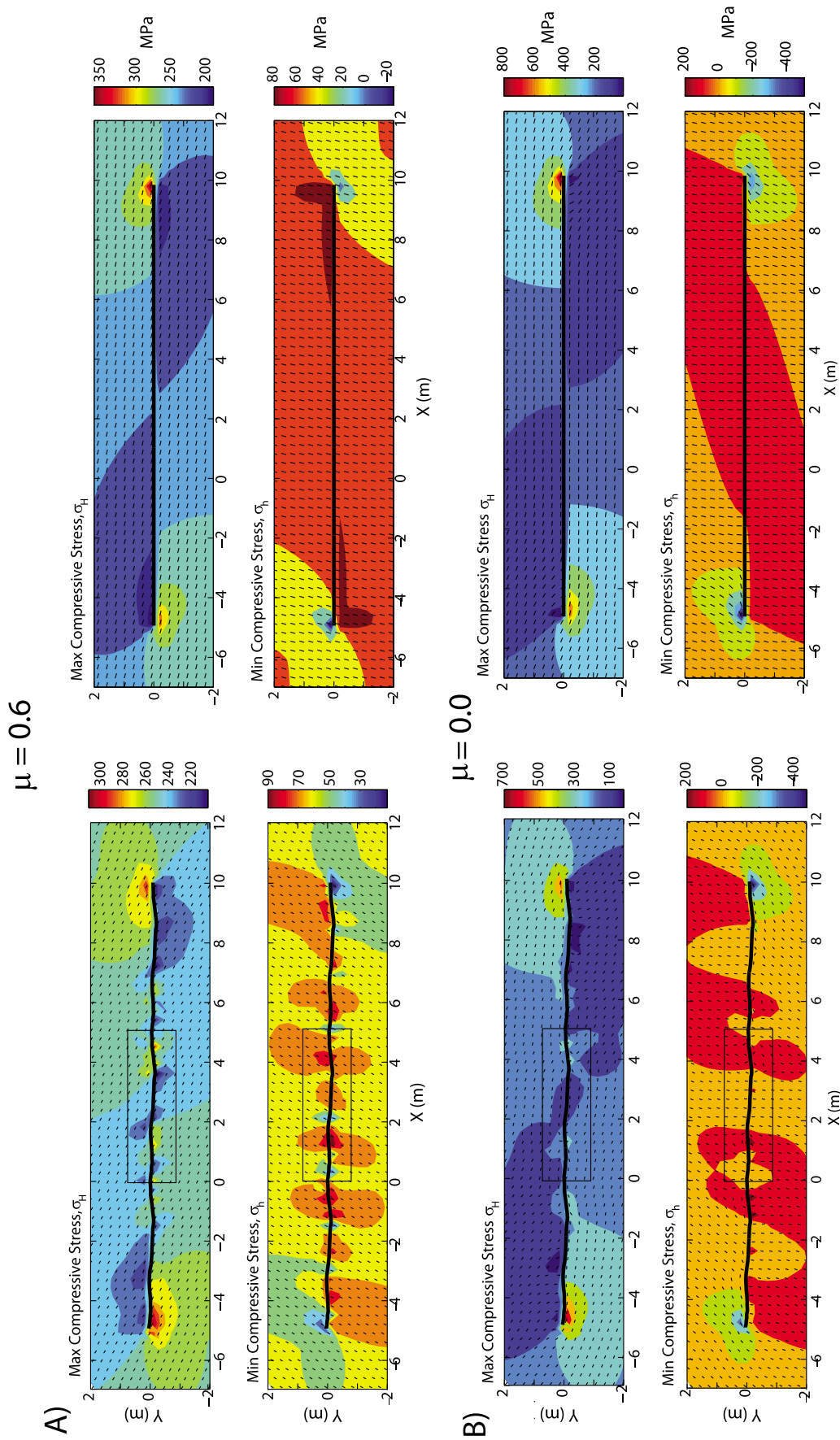


Figure 13. Comparison of maximum and minimum principal compressive stress fields for wavy and straight faults with constant coefficient of friction of (a) 0.6 and (b) 0.0. Hashed lines show the direction of each principal stress. Black boxes on wavy fault stress fields indicate the location of plots in Figure 14.

straight faults, little stress rotation (as defined by the eigenvectors of the local stress tensor relative to the remote stress tensor) is observed anywhere along the fault (Figure 14a). For the case of lubricated wavy faults, the maximum compressive stress is locally orthogonal to the fault in contractional bends and the differential stress very high (several hundred MPa) and parallel to the fault in extensional bends with lower differential stresses (<100–200 MPa) (Figure 14b). Figure 14c shows a close-up of the maximum compressive stress field around the portion of the Lobbia wavy fault where samples were taken for microstructural analysis. The vector field superimposed over the stress contours shows the direction of the maximum compressive stress. These are also the orientations at which tensile cracking would be expected. In general, the local orientation of the maximum compressive stress (for the lubricated fault) agrees surprisingly well with the microcrack orientation measurements shown in Figure 8.

4. Discussion

[29] The original motivation of this work was the field observation that melting on the Sierran wavy fault occurred in the presence of free fluids, implying that thermal pressurization on this fault did not preclude large temperature rises, at least not uniformly. This observation seems to be supported by microscopic evidence: PT is found in contractional jogs, where the traction normal to the fault (and as a consequence, heat rate production) is larger. Distribution of different fault rock assemblages is related to stress distribution along the fault. Significant opening occurred in the models (Figure 12) and is also preserved in the field exposures (Figures 1 and 2). As noted previously, this opening contributes to overall weakening of the fault by decreasing the effective local coulomb strength to zero. However, opening also tends to create large along-fault pressure differentials. This, coupled with observations of pooling of PT (Figure 6) in dilational reservoirs and thinning (Figure 5) in contractional bends (presumed main source of PT), suggests that significant fluid transport takes place along the fault, even on the small time scale of a single earthquake, implying that 1-D hydrothermal mechanical fault models that ignore such along-fault transport may be neglecting important terms. A number of such models [e.g., *Lachenbruch*, 1980; *Mase and Smith*, 1987; *Rice*, 2006; *Rempel and Rice*, 2006] have been used to explain the apparent paucity of frictional melts in the rock record by implying that for reasonable values of hydraulic conductivity, thermal pressurization should preclude melting. Significant gradients in along-fault fluid transport as evidenced here may necessitate considering a 2-D mass balance in such models. Results presented in this study, including microstructural observations along the Sierran wavy fault and opening calculations along the Lobbia wavy fault, suggest that fault nonplanarity can become an important factor controlling the spatial distribution of weakening mechanisms along a sliding fault.

[30] The Lobbia wavy fault is not self-affine. Interestingly, *Sagy et al.* [2007] found a power ~ 1 in the strike-parallel for some faults within the wavelength range of 10^{-4} – 10^{-2} . This was attributed to small-scale polishing during slip. This is a similar wavelength range on which extremely low power was observed along the Lobbia wavy fault. However, the Lobbia wavy fault showed moderate power ($\alpha \approx 2$) along the entire range of wavelengths examined. A possible cause of this smaller slope may be additional smaller wavelength roughness caused by preferential melting of lower melting point minerals such as biotite and variable amounts of wear due to differences in mineral indentation hardness [e.g., *Spray*, 1992; *Hirose and Shimamoto*, 2003]. The vast majority of data on roughness of natural fracture surfaces in rocks comes from sedimentary rocks which are mineralogically less diverse in terms of resistance to wear than the granitoid rocks of this study [e.g., *Power et al.*, 1987; *Lee and Bruhn*, 1996; *Sagy et al.*, 2007]. While the roughness data presented here consists of slip-parallel profiles taken from a single fault, this profile is unique among currently published roughness data because it comes from a PT-rich fault, and the fault surface is perfectly preserved, without any nonslip-related roughness induced either from weathering of the fault surface. Additional work is needed to establish whether the lower α calculated along the Lobbia wavy fault is a general feature of PT-rich faults or whether it is a slip-dependent phenomenon that exists in a limited bandwidth of wavelengths on PT-faults.

[31] Unfortunately, because the Lobbia wavy fault is not self-affine, it is difficult to directly compare the results of our study to the scaling results of *Dieterich and Smith* [2009]. What is notable, however, is that the roughness amplitude of the Lobbia wavy fault is near the upper bounds of those examined by *Dieterich and Smith* [2009], where roughness amplitudes greater than $\beta = 0.05$ resulted in greater than 50% reductions in maximum slip values relative to planar faults [*Dieterich and Smith*, 2009, Figure 4]. While the slip deficit in our study for $\mu = 0.6$ is also close to 50%, the deficit nearly disappears for the case of a lubricated ($\mu \approx 0.0$) fault. The inconsistency of the lubricated fault results in our study, relative to the results of *Dieterich and Smith* [2009], illustrate the combined importance of the remote stress tensor, the coefficient of friction on the fault elements, and opening on the fault for frictional slip on nonplanar faults. Various combinations of these parameters can be as (or more) important than fault roughness in controlling the slip distribution.

[32] The modeling results of our study also allow us to generalize the field observations from the Sierran and Lobbia wavy faults beyond the specific case of melting, and show that the effect of geometric barriers (waviness) on retarding slip is at least partially counteracted by (1) opening and (2) enhancement of temperature-related weakening mechanisms due to elevated normal stress in contractional bends. It follows that waviness in the case for the Lobbia fault does not preclude the achievement of low dynamic friction during slip,

Figure 14. Close-up view of stress field in area of the mapped Lobbia fault. White circles along the fault indicate the approximate location of each of the drilled samples. Black hashed lines are directions of maximum compressive stress, parallel to the orientation of potential tensile crack growth. (a) Stress field for $\mu = 0.6$ and (b) $\mu = 0.0$. (c) Blown up view of the sampling locations in Figure 14b. Stress directions with $\mu = 0.0$ are consistent with microcrack distributions measured in Figure 8.

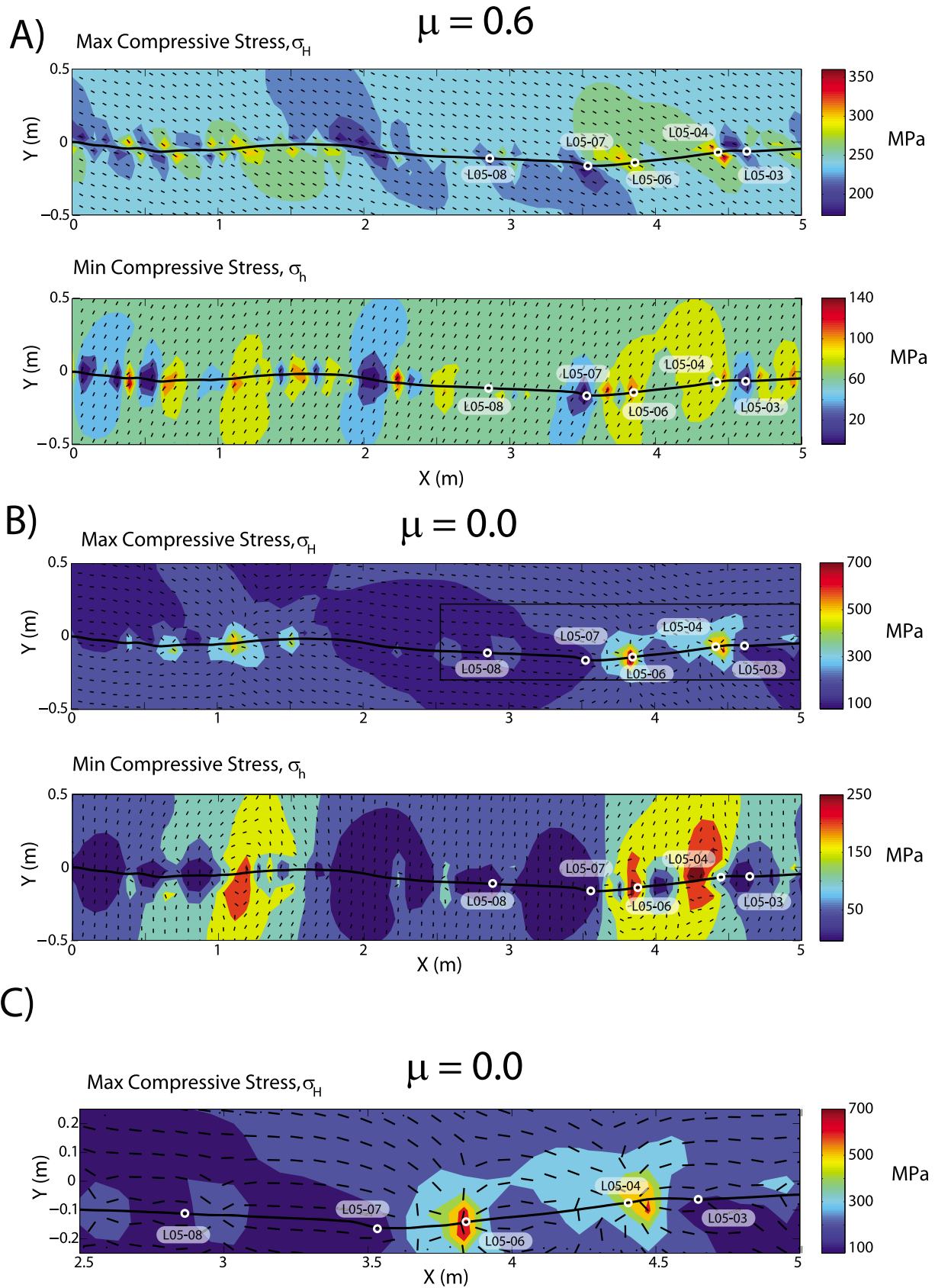


Figure 14

at least for the small slips discussed in this study. This is consistent with field estimates by *Di Toro et al.* [2006] and *Griffith et al.* [2009a], which suggested large stress drops based on coseismic slip/rupture lengths ratios. Moreover, since the Lobbia fault waviness is consistent with the waviness measured in nonsilicate rocks as limestones [e.g., *Sagy et al.*, 2007; *Candela et al.*, 2009], where other lubricating mechanisms are activated, [*Han et al.*, 2007], it seems that faults are lubricated during seismic slip even in the case of wavy faults.

[33] Weakening is accelerated in areas of enhanced normal stress. But how does this localized weakening affect the rest of the fault? Weakening and increased slip in areas of enhanced normal stress results in larger opening displacements along sections of the fault with reduced normal stress due to waviness. Because the walls of the fault are no longer in contact, friction effectively drops to zero there. In this way, localized weakening along wavy faults can be as effective in accelerating stress drop as homogeneous weakening across the entire fault. This implies that it is not unreasonable to extrapolate experimental results regarding frictional weakening to natural faults, as extreme weakening at a few points along a fault should be nearly equivalent to homogeneous weakening across an entire fault. If anything, since laboratory friction tests are typically performed at normal stresses far below those expected at asperities at seismogenic depths, laboratory friction tests may actually underestimate the overall weakening behavior of nonplanar faults at depth. It should be noted that because the simulations conducted in this study were quasistatic, the effect of opening at extensional jogs on stopping earthquake ruptures [e.g., *Sibson*, 1985] was not evaluated; however, there is nothing in the field to indicate that ruptures terminated near the extensional bends on the Lobbia wavy fault. The fact that PT fault veins are continuous across the entire Lobbia wavy fault suggests that the rupture which produced the observed melting did not terminate anywhere within the mapped profile.

[34] In addition to influencing weakening mechanisms, fault waviness appears to exert a strong control on off-fault damage. Of particular note is the apparent complexity of the off-fault damage along a fault, which is rather simple relative to mature crustal scale faults. This complexity appears to arise from the superposition of static stress effects due to fault nonplanarity and dynamic effects related to rupture propagation. Because the relative displacement across the fault is expected to be larger than several centimeters, the wall rocks are expected to have been transported through both contractional and extensional zones during seismic deformation, registering different or conflicting signatures of the inhomogeneous stress pattern across the fault bends. However, the dominant stress alterations due to fault nonplanarity are static in nature and increase with the amount of slip [*Chester and Chester*, 2000, Figure 13]. As a consequence, the strongest signature of nonplanarity corresponds to the final and current position of the wall rocks along the fault. Thus, microcracking related to nonplanarity stress alterations is expected to correlate well with the observed position of the rock samples. Indeed, the samples in this transitional zone (L05-04, L05-12) all contain a significant fracture set suborthogonal to the local fault strike, compatible with their observed and final position, as well as a second set oriented approximately 30°–45° from the local fault strike.

[35] Coseismic microcracks and secondary fractures may also be induced by a strong, quasi-singular transient stress during the passage of the fracture tip. Such a stress transient is not symmetric on either side of the fault [*Samudrala et al.*, 2002; *Di Toro et al.*, 2005b; *Griffith et al.*, 2009c] and may be extremely strong if rupture approaches the Rayleigh wave velocity [e.g., *Poliakov et al.*, 2002]. In the case of a right-lateral slip propagating from the west to the east, on a subvertical strike slip fault, tensile and compressive stress variations are expected in the southern and in the northern wall rocks, respectively. The stress surge associated with the rupture tip may be extremely strong and induce almost fault-parallel tension in the southern wall rocks when the rupture propagates close to the Rayleigh wave velocity. As a consequence, in addition to correlations of microcrack orientations with the position along fault bends, we expect fault-perpendicular cracking and fracturing to dominate on one side of the fault (i.e., in the southern wall consistent with the findings of *Di Toro et al.* [2005b]). This seems to be the case for pseudotachylite injection veins observed at the outcrop (Figure 1b) and at the microscale, as the majority of pseudotachylite injection veins are found on the south side of the fault [*Di Toro et al.*, 2005b]. On the basis of several studies [*Samudrala et al.*, 2002; *Di Toro et al.*, 2005b; *Griffith et al.*, 2009c] and given that the fault slipped right-laterally, this observation would imply that the paleorupture direction was from west to east.

[36] However, this is not the case for the microcracks measured in quartz grains away from the fault as no systematic difference in either microcrack orientation or density is observed north and south of the fault. The only systematic differences occur parallel to the fault and appear to be related to the irregular fault geometry. Hence we may conclude that the injection veins record preferentially the dynamic stress surge, while the microcracks in quartz rather record the static stress perturbation due to nonplanar fault geometry.

[37] This seems to infer that fracture damage associated with passage of a dynamic shear rupture tip (at least at depths on the order of 10 km) is likely confined to the sliding plane, as all injection veins indeed grow from the fault surface. This observation is certainly in agreement with experimental studies [*Samudrala et al.*, 2002; *Griffith et al.*, 2009c], in which mode I cracks nucleated on a rupture interface due to the transient perturbation of a moving mode II shear rupture. The reason for this limitation of dynamic damage to the fault surface is not immediately clear but is likely due to a combination of factors including relief of the transient stress perturbation due to initial crack formation immediately adjacent to the rupture plane and large lithostatic loads opposing crack opening [e.g., *Ben-Zion and Shi*, 2005; *Finzi et al.*, 2009]. In any case, the observations of microcrack distribution and orientation speak to the complexity of off-fault damage, even along faults whose history is relatively simple relative to active crustal scale faults.

[38] A significant limitation of this investigation is the small strain assumption in the modeling technique. Given that field observations only allow information about the final deformed state of the faults, this assumption is important. However, a systematic study of the phenomena discussed here using an approach that allows for large strains [e.g., *Griffith et al.*, 2009b] would likely clarify some of the

uncertainty of conclusions regarding the interplay of fault waviness, frictional processes, and off-fault deformation.

5. Conclusions

[39] Fault waviness taken from a natural field example of a seismogenic fault exhumed from ~10 km depth results in heterogeneous melting distribution along strike due to enhanced normal stress in contractional bends. Field and theoretical evidence suggests that melting (enhanced weakening) in contractional bends is accompanied by opening in extensional bends. Modeling suggests that enhanced weakening combined with opening makes the fault equivalent to a homogeneously weak straight fault of equal length. Heterogeneous normal traction and opening also creates large along-strike pressure gradients along the faults, meaning that along-fault fluid transport becomes very important during faulting. This is supported by apparent mobility of pseudotachylytes that accumulate in opening reservoirs. Increasing slip and opening distributions due to enhanced weakening mirror longer wavelength roughness, highlighted by broader stress concentrations and more wide-spread opening compared to smaller slip cases.

[40] Even with enhanced weakening, there is still a slip deficit on wavy faults, under the same overall stress drop. However, the slip deficit decreases as the magnitude of slip increases. This implies that fault waviness is more important as the frictional strength of a fault (defined as the sliding coefficient of friction) increases. Once significant weakening along high-stress patches occurs, however, the slip distribution on the fault, aided by additional weakening by fault opening, is virtually indistinguishable from a fault with a uniformly low coefficient of friction.

[41] Slip on wavy faults is accompanied by a strongly heterogeneous stress field. For faults on which the friction coefficient is very low (i.e., the fault is lubricated) this implies significant rotation of the local principle stresses. Numerical mechanical modeling reveals that damage in the form of intragranular microcracks is strongly tied to the static stress distribution rather than the transient stress field associated with earthquake rupture propagation. Damage at seismogenic depths (~10 km) due to transient stresses associated with rupture propagation appears to be limited to areas very close to the fault. Further understanding of all of these phenomena can be gained by extending the modeling approach to allow for large strains.

Appendix A: Field and Microstructural Measurements and Mesh Creation

[42] The boundaries of the pseudotachylyte fault vein and clasts within the fault were digitized at an average spacing of ~3 mm, producing a high precision digital map of the relevant fault structures. PT area (Figure 2a) is calculated using a Matlab script, which imports the digital fault geometry and subtracts the clast area from the total area between the upper and lower fault surfaces. Average PT thickness is calculated by dividing the area by the total straight-line (x parallel) length of the fault profile; however, the fault thickness profile (Figure 2b) is generated by measuring the y parallel distance between the upper and lower fault surfaces after manually

removing the injection veins. This is done to differentiate between the purposes of measuring the average PT thickness and the thickness distribution, as the average PT thickness is used below as an indicator of PT volume, while the thickness distribution is used as a measure of coseismic fault opening displacement.

[43] Microcracks generated in situ were differentiated from cracking due to sample preparation by the presence or absence of fluid inclusion trails. Microcracks in the quartz grains were discretized by tracing the digital images (Figures 7e and 7f). The resulting discretized curves consist of nodes whose orientation is described by position vectors in a local reference frame, and these nodes are connected by discrete subequal length segments (individual segments are approximately 50–100 μm long). In practice, each digitized fracture typically consists of between 3 and 30 individual segments, depending on fracture length. For orientation data, rather than measuring a representative trend for each individual fracture, we measured and recorded the orientation of each individual segment and plotted all of the data for each sample on a rose diagram (Figure 8). This approach has two distinct advantages over the traditional approach of representing each fracture with a single measurement: (1) the inherent nonplanarity of the microcracks is preserved and (2) longer cracks, which are made up of more segments than shorter cracks, are given more weight. Microcrack density was measured and calculated using an expression of the two-dimensional nondimensional fracture density Γ :

$$\Gamma = \frac{1}{A} \sum_{i=1}^N a_i^2, \quad (\text{A1})$$

where A is the total quartz grain area for each set of measurements, and a_i is the half-length of the i th microcrack. For the calculation of fracture density, we use the total half-length of each microcrack rather than the length of each individual segment. For quartz grains with saturated regions of microcracks (e.g., Figure 7b), the measured fracture density is probably an underestimate, as it is difficult to distinguish individual microcracks in these regions.

[44] Unlike the digitized fault maps created for PT area and thickness and fault roughness calculations, a separate digital map was created in which the fault is idealized as a curvilinear. The line is traced on top of the fault map, and some minor qualitative interpretation is necessary along sections of the fault where PT is particularly thick, i.e., where significant opening has taken place. For the Lobbia wavy fault ($L = 4.98$ m), this process yielded a mean spacing of digitized points of $dt = 0.003$ m, much finer than the half-wavelength (~0.05 m) of the smallest curve that could be deciphered with confidence from the fault map. For the boundary element analysis, it is desirable to have elements of subequal length. We resample the fault by linear interpolation such that each element has length ($dt = 0.009$ m) greater than the mean spacing of points ($dt_{\text{ave}} = 0.003$ m) in the original fault. The fault mesh is smoothed further using a fifth-order low-pass filter which removes any roughness with wavelength less than 0.010 m. This filter ensures that our fault digitization process does not introduce any artificial high-frequency roughness to the fault. This process yields a fault mesh with 1505 elements for the Lobbia wavy fault. The 0.009 m spacing allows all

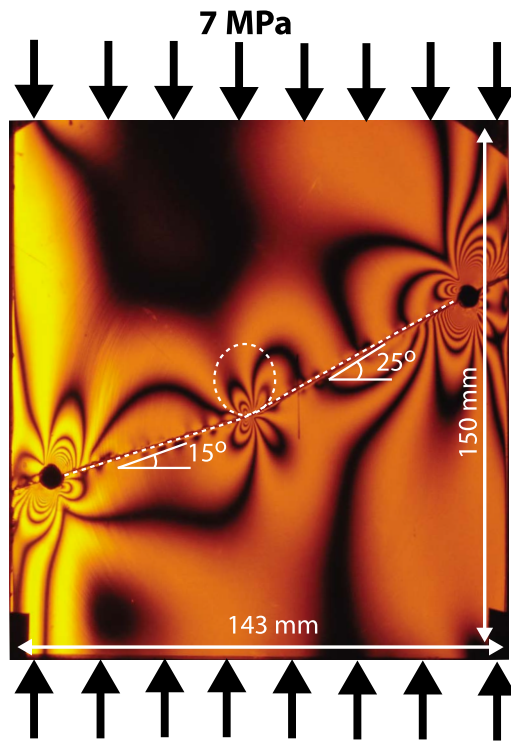


Figure B1. Static photoelastic experiment on a fault bend in a 8 mm thick sheet of CR-39 Columbia Resin. Bend of radius 14 mm (dashed circle) separates a straight segment inclined at 15° from a segment inclined at 25° . Steel pegs inserted at either end of the fault interface fixes the finite length of the fault. The sample is loaded by a vertical uniaxial load of 7 MPa, and the resulting fringe pattern is proportional to contours of maximum shear stress. The region in the white box is compared to numerical calculations in Figure B2.

features on the fault to be represented smoothly, yet allows for reasonably fast computation time.

Appendix B: BEM Code

[45] The BEM code utilized in this study has been validated for straight faults with nonhomogeneous friction by *Mutlu and Pollard* [2008]. Here we confirm the model results for nonplanar fault geometries by comparing numerical results to photoelastic laboratory scale models. We apply a uniform uniaxial load of 7 MPa to a $143 \text{ mm} \times 150 \text{ mm} \times 8 \text{ mm}$ sheet of CR-39 Columbia Resin (Figure B1) with relevant static properties Young's Modulus ($E = 2 \text{ GPa}$), poisson's ratio ($\nu = 0.43$), and stress optical constant ($c_\sigma = 0.013 \text{ MPa m}$) [e.g., *Dally and Lewis*, 1968]. The CR-39 specimen is cut at an angle 15° to the horizontal on the left side, curving to an angle of 25° through a bend with radius of curvature $R = 14 \text{ mm}$ centered at 67.6 mm from the left. The sample interface is lubricated with a thin film of petroleum jelly. Steel pins along the interface near each respective vertical specimen boundary, enforcing a zero slip boundary condition and approximating a finite-length bent fracture between the two pins. A sodium lamp (wavelength, $\lambda = 589 \text{ nm}$) is used as a monochromatic light source, and the sample is placed between two circular polarizers. The resulting interference pattern is pictured in Figure B1. The stiffness contrast between the CR-39

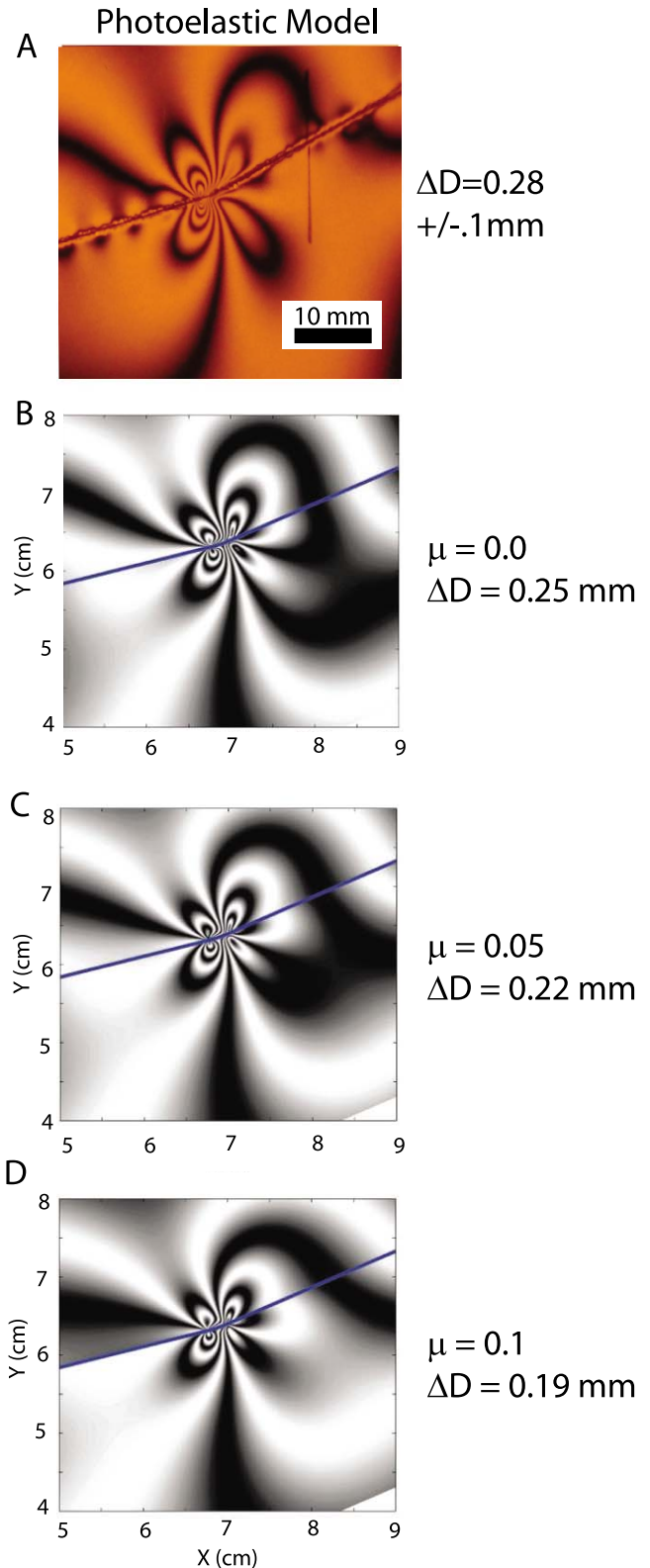


Figure B2. (a) Comparison of experimental fringe patterns with theoretical calculations for faults of uniform frictional resistance governed by static friction coefficient of (b) $\mu = 0$, (c) $\mu = 0.05$, and (d) $\mu = 0.1$.

and the steel pins results in a large stress concentration, however the bend is located sufficiently far away to be largely unaffected. For model comparison purposes, we focus on a region 40 mm square centered around the fault bend (white box, Figure B1). A vertical straight line drawn 83 mm from the left model boundary is used to measure the slip.

[46] We calculate slip on a curved fault with identical geometry embedded in an infinite elastic medium under plane stress conditions. Length of individual elements in the numerical fault mesh are approximately 1 mm, making the ratio between mesh coarseness and radius of curvature similar to that for the smallest wavelength roughness in the Lobbia wavy fault simulations. The experimental fault interface is lubricated, but the exact effective coefficient of friction is not known, so we present three simulations with $\mu = 0$, 0.05, and 0.1, respectively, to cover a reasonable range of values. These values for static friction yield slip at $x = 0.83$ mm of 0.25, 0.22, and 0.19 mm versus a measured value of 0.28 ± 0.1 mm. The stress field calculated around the model fault can be calculated using the stress optic law:

$$\bar{N} = \frac{h}{f}(\sigma_1 - \sigma_2), \quad (\text{B1})$$

where \bar{N} is the fringe order, h is the thickness, and f is the stress optical coefficient of the CR-39 plate. The calculated fringe order is converted to a light intensity (I) image by the equation of two beam interference

$$I = \cos^2(\pi\bar{N}), \quad (\text{B2})$$

and plotted below the experimental result in Figure B2.

[47] As noted above, the slip value for all of the friction cases fall within error of the value measured in the experimental case. In all cases there is also a small amount (<0.05 mm) of opening at the fault bend; however, this value is too small to be observed in the experimental case. The calculated fringe patterns are all qualitatively very similar to the experimental case with slight variations. The fringe lobes to the left of the fault bend are best matched by the $\mu = 0$ case, whereas the fringes to the right of the bend are best matched by the higher friction cases. In addition, there are some periodic stress concentrations along the section of the experimental fault inclined at 15° to the left of the fault which are not captured in the numerical simulations. These are likely due to heterogeneous friction distributed along the model interface. The cause of this heterogeneity is unclear but is likely related to roughness of the machined interface surface and pinching of the lubricant along the interface. In any case, despite the inherent ambiguity of the boundary conditions along the experimental fault interface, the numerical method satisfactorily reproduced (1) the slip and (2) the stress field near the fault bend.

[48] **Acknowledgments.** This work was supported by National Science Foundation grant OISE-0754258 to Griffith and European Research Council Starting grant project 205175 (USEMS) to Di Toro. Di Toro and Nielsen were also partially supported by a Progetti di Eccellenza Fondazione Cassa di Risparmio di Padova e Rovigo (CARIPARO). Analytical work was conducted in the HT-HP lab at the Istituto Nazionale di Geofisica e Vulcanologia. Leonardo Tauro and Elena Masiero prepared the thin sections for the Lobbia wavy fault samples. Sefano Castelli orthorectified the field photos for the photomosaic. Giorgio Pennacchioni, Silvia Mitterberger, and Andrea Bistacchi are thanked for help and insightful discussions in the field.

References

- Ben-Zion, Y., and Z. Shi (2005), Dynamic rupture on a material interface with spontaneous generation of plastic strain in the bulk, *Earth Planet. Sci. Lett.*, **236**, 486–496, doi:10.1016/j.epsl.2005.03.025.
- Berger, P., and A. M. Johnson (1980), First-order analysis of deformation of a thrust sheet moving over a ramp, *Tectonophysics*, **70**, T9–T24.
- Bhat, H. S., R. Dmowska, J. R. Rice, and N. Kame (2004), Dynamic slip transfer from the Denali to Totschunda faults, Alaska: Testing theory for fault branching, *Seismol. Soc. Am. Bull.*, **94**, S202–S213.
- Brodsky, E. E., and H. Kanamori (2001), Elastohydrodynamic lubrication of faults, *J. Geophys. Res.*, **106**(B8), 16,357–16,374.
- Candela, T., F. Renard, M. Bouchon, A. Brouste, D. Marsan, J. Schmittbuhl, and C. Voisin (2009), Characterization of fault roughness at various scales: Implications of three-dimensional high resolution topography measurements, *Pageoph*, **166**, doi:10.1007/s00024-009-0521-2.
- Carslaw, H. S., and J. C. Jaeger (1959), *Conduction of Heat in Solids*, 2nd ed., Clarendon Press, Oxford.
- Chester, J. S., and R. C. Fletcher (1997), Stress distribution and failure in anisotropic rock near a bend on a weak fault, *J. Geophys. Res.*, **102**, 693–708.
- Chester, J. S., and F. M. Chester (2000), Stress and deformation along wavy frictional faults, *J. Geophys. Res.*, **105**, 23,421–23,430.
- Cooke, M. L., and A. Kameda (2002), Mechanical fault interaction in the Los Angeles Basin: A two-dimensional analysis using mechanical efficiency, *J. Geophys. Res.*, **107**(B7), 2146, doi:10.1029/2001JB000542.
- Crouch, S. L. (1976), Solution of plane elasticity problems by the displacement discontinuity method, *Int. J. Num. Meth. Eng.*, **10**, 301–343.
- Dally, J. W., and D. Lewis (1968), A photoelastic analysis of propagation of Rayleigh waves past a step change in elevation, *Seismol. Soc. Am. Bull.*, **58**, 539–563.
- De Bremaecker, J. C., and M. C. Ferris (2004), Numerical models of shear fracture propagation, *Int. J. Fract.*, **21**, 2161–2178.
- De Bremaecker, J. C., M. C. Ferris, and D. Ralph (2000), Compressional fractures considered as contact problems and mixed complementarity problems, *Eng. Fract. Mech.*, **66**, 287–303.
- Del Gaudio, P., G. Di Toro, R. Han, T. Hirose, S. Nielsen, T. Shimamoto, and A. Cavallo (2009), Frictional melting of peridotite and seismic slip, *J. Geophys. Res.*, **114**, B06306, doi:10.1029/2008JB005990.
- Di Toro, G., and G. Pennacchioni (2004), Superheated friction-induced melts in zoned pseudotachylytes within the Adamello tonalites (Italian Southern Alps), *J. Struct. Geol.*, **26**, 1783–1801.
- Di Toro, G., and G. Pennacchioni (2005), Fault plane processes and mesoscopic structure of a strong-type seismogenic fault in tonalites (Adamello batholith, Southern Italian Alps), *Tectonophysics*, **402**, 55–80.
- Di Toro, G., G. Pennacchioni, and G. Teza (2005a), Can pseudotachylytes be used to infer earthquake source parameters? An example of limitations in the study of exhumed faults, *Tectonophysics*, **402**, 3–20.
- Di Toro, G., S. Nielsen, and G. Pennacchioni (2005b), Earthquake rupture dynamics frozen in exhumed ancient faults, *Nature*, **436**, 1009–1012.
- Di Toro, G., T. Hirose, S. Nielsen, G. Pennacchioni, and T. Shimamoto (2006), Natural and experimental evidence of melt lubrication of faults during earthquakes, *Science*, **311**, 647–649.
- Dieterich, J. H., and D. E. Smith (2009), Nonplanar faults: mechanics of slip and off-fault damage, *Pure. Appl. Geophys.*, **166**, 1799–1815, doi:10.1007/s00024-009-0517-y.
- Evans, J. P., Z. K. Shipton, M. A. Pachell, S. J. Lim, and K. Robeson (2000), The structure and composition of exhumed faults, and their implications for seismic processes, in *Third Conference on Tectonic Problems of the San Andreas Fault System*, vol. 21, edited by G. Bokelmann and R. L. Kovach, pp. 67–81, Stanford University Publications.
- Finzi, Y., E. H. Hearn, Y. Ben-Zion, and V. Lyakhovsky (2009), Structural properties and deformation patterns of evolving strike-slip faults: Numerical simulations incorporating damage rheology, *Pure. Appl. Geophys.*, **166**, 1537–1573, doi:10.1007/s00024-009-519-9.
- Griffith, W. A., G. Di Toro, G. Pennacchioni, and D. D. Pollard (2008), Thin pseudotachylytes in faults of the Mt. Abbot Quadrangle, Sierra Nevada California: Physical constraints on seismic slip, *J. Struct. Geol.*, **30**, 1086–1094, doi:10.1016/j.jsg.2008.05.003.
- Griffith, W. A., G. Di Toro, G. Pennacchioni, D. D. Pollard, and S. Nielsen (2009a), Static stress drop associated with brittle slip events on exhumed faults, *J. Geophys. Res.*, **114**, B02402, doi:10.1029/2008JB005879.
- Griffith, W. A., P. F. Sanz, and D. D. Pollard (2009b), Influence of outcrop scale fractures on the effective stiffness of fault damage zone rocks, *Pure. Appl. Geophys.*, **166**, 1595–1627, doi:10.1007/s00024-009-519-9.
- Griffith, W. A., A. J. Rosakis, D. D. Pollard, and C.-W. Ko (2009c), Dynamic rupture experiments elucidate tensile crack development during propagating earthquake ruptures, *Geology*, **37**, 795–798, doi:10.1130/G30064A.

- Han, R., T. Shimamoto, T. Hirose, J.-H. Ree, and J. Ando (2007), Ultralow friction of carbonate faults caused by thermal decomposition, *Science*, *316*, 878–881.
- Heaton, T. H. (1990), Evidence for and implications of self-healing pulses of slip in earthquake rupture, *Phys. Earth Planet. Interiors*, *64*, 1–20.
- Hirose, T., and T. Shimamoto (2003), Fractal dimension of molten surfaces as a possible parameter to infer the slip-weakening distance of faults from natural pseudotachylytes, *J. Struct. Geol.*, *25*(10), 1569–1574.
- Kame, N., J. R. Rice, and R. Dmowska (2003), Effects of prestress state and rupture velocity on fault branching, *J. Geophys. Res.*, *108*(B5), 2265, doi:10.1029/2002JB002189.
- Kirkpatrick, J. D., and Z. K. Shipton (2009), Geologic evidence for multiple slip weakening mechanisms during seismic slip in crystalline rock, *J. Geophys. Res.*, *114*, B12401, doi:10.1029/2008JB006037.
- Kirkpatrick, J. D., Z. K. Shipton, J. P. Evans, S. Micklethwaite, and S. J. Lim (2008), Strike-slip fault terminations at seismogenic depths: The structure and kinematics of the Glacier Lakes fault, Sierra Nevada United States, *J. Geophys. Res.*, *113*, B04304, doi:10.1029/2007JB005311.
- Lachenbruch, A. H. (1980), Frictional heating, fluid pressure, and the resistance to fault motion, *J. Geophys. Res.*, *85*, 6,097–6,112.
- Lee, J.-J., and R. L. Bruhn (1996), Structural anisotropy of normal fault surfaces, *J. Struct. Geol.*, *18*, 1043–1059.
- Martel, S. J., D. D. Pollard, and P. Segall (1988), Development of simple strike-slip fault zones, Mount Abbot Quadrangle, Sierra Nevada, California, *Geol. Soc. Am. Bull.*, *100*, 1451–1465.
- Mase, C. W., and L. Smith (1987), Effects of frictional heating on the thermal, hydrologic, and mechanical response of a fault, *J. Geophys. Res.*, *92*, 6249–6272.
- Melosh, J. (1996), Dynamic weakening of faults by acoustic fluidization, *Nature*, *397*, 601–606.
- Mijar, A. R., and J. S. Arora (2000), Review of formulations for elastostatic frictional contact problems, *Struct. Multidisciplinary Optim.*, *20*, 167–189.
- Mutlu, O., and D. D. Pollard (2008), On the patterns of wing cracks along an outcrop scale flaw: A numerical modeling approach using complementarity, *J. Geophys. Res.*, *113*, B06403, doi:10.1029/2007JB005284.
- Nielsen, S., and L. Knopoff (1998), The equivalent strength of geometrical barriers to earthquakes, *J. Geophys. Res.*, *103*, 9953–9965.
- Nielsen, S., G. Di Toro, T. Hirose, and T. Shimamoto (2008), Frictional melt and seismic slip, *J. Geophys. Res.*, *113*, B01308, doi:10.1029/2007JB005122.
- Okubo, P. G., and J. H. Dieterich (1984), Effects of fault properties on frictional instabilities produced on simulated faults, *J. Geophys. Res.*, *89*, 5,817–5,827.
- Pachell, M. A., and J. P. Evans (2002), Growth, linkage, and termination processes of a 10-km-long, strike-slip fault in jointed granite: the Gemini fault zone, Sierra Nevada, California, *J. Struct. Geol.*, *24*(12), 1903–1924.
- Parsons, T. (2007), Persistent earthquake clusters and gaps from slip on irregular faults, *Nature Geoscience*, *1*, 59–63.
- Poliakov, A. N. B., R. Dmowska, and J. R. Rice (2002), Dynamic Shear rupture interactions with fault bends and off-axis secondary faulting, *J. Geophys. Res.*, *107*(B11), 2295, doi:10.1029/2001JB000572.
- Power, W. L., J. Tullis, S. R. Brown, G. N. Boitnott, and C. H. Scholz (1987), Roughness of natural fault surfaces, *Geophys. Res. Lett.*, *14*, 29–32.
- Power, W. L., T. E. Tullis, and J. D. Weeks (1988), Roughness and wear during brittle faulting, *J. Geophys. Res.*, *93*, 15,268–15,278.
- Rempel, A. W., and J. R. Rice (2006), Thermal pressurization and the onset of melting in fault zones, *J. Geophys. Res.*, *111*, B09314, doi:10.1029/2006JB004314.
- Resor, P. G., and V. E. Meer (2009), Slip heterogeneity on a corrugated fault, *Earth Planet. Sci. Lett.*, *288*, 483–491, doi:10.1016/j.epsl.2009.10.010.
- Rice, J. R. (2006), Heating and weakening of faults during earthquake slip, *J. Geophys. Res.*, *111*, B05311, doi:10.1029/2005JB004006.
- Sagy, A., and E. E. Brodsky (2009), Geometric and Rheological Asperities in an Exposed Fault Zone, *J. Geophys. Res.*, *114*, B02301, doi:10.1029/2008JB005701.
- Sagy, A., E. E. Brodsky, and G. J. Axen (2007), Evolution of fault-surface roughness with slip, *Geology*, *35*, 283–286.
- Samudrala, O., Y. Huang, and A. J. Rosakis (2002), Subsonic and intersonic shear rupture of weak planes with a velocity weakening cohesive zone, *J. Geophys. Res.*, *107*(B8), 2170, doi:10.1029/2001JB000460.
- Saucier, F., E. Humphreys, and R. Weldon (1992), Stress near geometrically complex strike-slip faults: application to the San Andreas fault at Cajon Pass, Southern California, *J. Geophys. Res.*, *97*, 5081–5094.
- Segall, P., and D. D. Pollard (1983), Nucleation and growth of strike-slip faults in granite, *J. Geophys. Res.*, *88*, 555–568.
- Sibson, R. H. (1974), Frictional constraints on thrust, wrench and normal faults, *Nature*, *249*, 542–545.
- Sibson, R. H. (1985), Stopping of earthquake ruptures at dilational fault jogs, *Nature*, *316*, 248–251, doi:10.1038/316248a0.
- Spray, J. G. (1992), A physical basis for the frictional melting of some rock forming minerals, *Tectonophysics*, *204*, 205–221.
- Warr, L. N., B. A. van der Pluijm, D. R. Peacor, and C. M. Hall (2003), Frictional melt pulses during a 1.1 Ma earthquake along the Alpine Fault, New Zealand, *Earth Planet. Sci. Lett.*, *209*(1–2), 39–52, doi:10.1016/S0012-821X(03)00070-0.

G. Di Toro, S. Nielsen, and S. A. F. Smith, Istituto Nazionale di Geofisica e Vulcanologia, Via di Vigna Murata, 605, 00143, Rome, Italy.
 W. A. Griffith, Department of Geology and Environmental Science, University of Akron, Akron, OH 44303-4101, USA. (wag8@uakron.edu)